Motion limiting nonlinear dynamics of initially curved beams

Hamed Farokhi [a], Mergen H. Ghayesh [b,*]

[a] *Department of Mechanical and Construction Engineering, Northumbria University, Newcastle upon Tyne NE1 8ST, UK*
[b] *School of Mechanical Engineering, University of Adelaide, South Australia 5005, Australia*
**Corresponding author: mergen.ghayesh@adelaide.edu.au*
Email: (H Farokhi): hamed.farokhi@northumbria.ac.uk

Abstract

An initially curved beam is considered and its motion is constrained using two elastic constraints; the corresponding non-smooth nonlinear transverse dynamics is investigated for the first time. A clamped-clamped beam with one axially movable end is modelled via Bernoulli-Euler beam theory together with the inextensibility condition, giving rise to nonlinear inertial terms along with nonlinear geometric terms. Furthermore, the damping is modelled via Kelvin-Voigt internal damping model. The proposed model is verified for linear and nonlinear behaviours via comparison to a finite element model. The impact between beam and constraints is incorporated via calculating its work contribution. The nonlinear equation of motion is derived while incorporating geometric, damping, inertial, and constraints nonlinearities. A series of spatial basis functions together with corresponding vibration modes are used as the proposed solution of the transverse displacement. A modal discretisation is performed via the weighted-residual method of Galerkin and the corresponding non-smooth terms are kept intact while conducting numerical integration. A numerical continuation technique is utilised to solve the resultant equations. The non-smooth response is obtained for various cases and the effects of several parameters are studied thoroughly.

Keywords: motion limiting; initially curved; beam; nonlinear; dynamics

1. Introduction

Beams/plates/shells [1-6] are the most common continuous structures present in different mechanical and civil applications [7-21]. Dynamical flexible systems such as beams subject to motion constraints, as a concept, have been examined for over few decades, due to their applications in systems having impact, friction, and backlash. With emergence of new applications of this class, such as vibration energy harvesters, this topic is gaining further attention from researchers. Additionally, in many applications the contact and impact between neighbouring elements is undesirable, which signifies the importance of analysing the dynamical behaviour of beam structures in contact with motion constraints.

A common dynamical system subject to motion constraints is a set of spring-mass-damper system subject to spatial barriers. The early investigations on this class [22-25] were conducted by: Nigm and Shabana [26], who performed a vibration analysis theoretically and obtained steady-state responses in the presence of an impact damper; Choi and Noah [27], who conducted an examination into the force-oscillation characteristics of a one-degree-of-freedom system with a piecewise linear stiffness; Natsiavas [25], who analysed the effect of bilinear stiffness and damping on the dynamical behaviour of oscillators. Further investigations were conducted by Pilipchuk [28] who studied the nonlinear dynamics of nonlinear vibrations of damped oscillators subject to nonsmooth limits. Charroyer et al. [29] studied the nonlinear self-excited oscillation of systems under friction-induced vibration; they utilised a time integration method together with a shooting method to correctly shooting technique to correctly estimate the growing oscillations.

The mass-spring-damper models were replaced by continuous systems such as beams [30, 31], for instance by Björkenstam [30], who examined the dynamical stability of a periodically excited bar subject to a constraint. Further investigation was conducted Metallidis and Natsiavas [32] who studied the longitudinal vibration of a periodically excited constrained rod. Issanchou et al. [33] studied conducted numerical and experimental investigations on the motion of a damped string against an obstacle; they employed a modal-based method study the system response numerically and compared it to experimental observations.

One prominent application of motion limiting dynamics of beams or spring-mass-damper systems is in vibration energy harvesters where the kinetic (motion) energy is converted efficiently into electrical power. The motion is limited in some vibration energy harvesters to broaden the frequency bandwidth, and hence to improve the performance. There is, however, a compromise between the effective frequency band and the amount of generated power. Liu et al. [34] employed a piezoelectric energy transduction method to and a cantilever stopper to propose an energy harvester in a microscale level. Soliman et al. [35] proposed a new model for an energy harvester based on a motion-limiting constraints for frequency bandwidth widening purposes.

This study is the *first* to investigate the motion limiting non-smooth nonlinear dynamics of initially curved beams. Various nonlinearities are retained in model development and numerical simulations. The motion constraints are modelled via nonlinear springs. The Kelvin-Voigt model is utilised for more accurate modelling of energy dissipation. The centreline inextensibility is used due to one end of the clamped-clamped beam being axially movable. The resultant nonlinear equation, consisting of nonlinear terms of

geometric, damping, inertial, and piecewise types is discretised making use of the method of Galerkin. The developed model and numerical technique are verified via comparison to three-dimensional nonlinear finite element analysis. Thorough numerical simulations are conducted and the effects of various parameters are examined. Amplitude-frequency curves are constructed as well as phase plane plots and time histories.

2. Continuous model for motion limiting dynamics of beams

Shown in Fig. 1 is an initially curved doubly-clamped beam with right-hand side end free to move axially. The length of the initially curved beam is L; the thickness and width are denoted by h and b, respectively. There are two elastic constraints positioned at both sides of the beam in the transverse direction (i.e. z), with gap g_0 from the axial axis (i.e. x), as shown in Fig. 1. The constrained beam system is under base excitation in the form of $z_0 \sin(\Omega t)$, where Ω and z_0 represent the frequency and amplitude of the base excitation, respectively. It should be noted that the elastic constraints are under base excitation as well, i.e. it is assumed that the whole system is subject to base excitation. The shape of the initial curvature of the beam is represented by $w_0(x)$.

The constrained system undergoes both longitudinal and transverse motions. The longitudinal motion is represented by $u(x,t)$. The total displacement in the z direction of the beam is denoted by $v(x,t)$. Denoting the transverse motion relative to the clamped base by $w(x,t)$, the total transverse displacement can be formulated as $v(x,t)= w(x,t)+ z_0 \sin(\Omega t)$.

One important characteristics of a beam with one axially movable end is that the centreline remains inextensible. The centreline inextensibility condition relates the

longitudinal displacement and the rotation angle of the centreline to the transverse displacement. Hence, the axial strain in the beam can be formulated as

$$\varepsilon = -z\left[\frac{\partial^2 w}{\partial x^2} + \frac{\mathrm{d}w_0}{\mathrm{d}x}\frac{\mathrm{d}^2 w_0}{\mathrm{d}x^2}\frac{\partial w}{\partial x} + \frac{1}{2}\left(\frac{\mathrm{d}w_0}{\mathrm{d}x}\right)^2\frac{\partial^2 w}{\partial x^2} + \frac{\mathrm{d}w_0}{\mathrm{d}x}\frac{\partial w}{\partial x}\frac{\partial^2 w}{\partial x^2} + \frac{1}{2}\left(\frac{\partial w}{\partial x}\right)^2\left(\frac{\partial^2 w}{\partial x^2} + \frac{\mathrm{d}^2 w_0}{\mathrm{d}x^2}\right)\right], \tag{1}$$

where z is the vertical distance from the centreline.

The motion energy of the constrained system consists of the transverse motion as well as the longitudinal motion, and can be formulated as

$$T = \frac{1}{2}\rho A\int_0^L\left[\left(z_0\Omega\cos(\Omega t) + \frac{\partial w}{\partial t}\right)^2 + \left(\int_0^x\left(\frac{\partial w}{\partial x} + \frac{\mathrm{d}w_0}{\mathrm{d}x}\right)\frac{\partial^2 w}{\partial x\partial t}\mathrm{d}x\right)^2\right]\mathrm{d}x, \tag{2}$$

in which ρ is density and A is the area of the cross-section.

The elastic strain energy of the beam can be written as

$$\begin{aligned}\Pi = \frac{1}{2}EI\int_0^L\Bigg[&\frac{\partial^2 w}{\partial x^2} + \frac{\mathrm{d}w_0}{\mathrm{d}x}\frac{\mathrm{d}^2 w_0}{\mathrm{d}x^2}\frac{\partial w}{\partial x} + \frac{1}{2}\left(\frac{\mathrm{d}w_0}{\mathrm{d}x}\right)^2\frac{\partial^2 w}{\partial x^2}\\ &+ \frac{\mathrm{d}w_0}{\mathrm{d}x}\frac{\partial w}{\partial x}\frac{\partial^2 w}{\partial x^2} + \frac{1}{2}\left(\frac{\partial w}{\partial x}\right)^2\left(\frac{\partial^2 w}{\partial x^2} + \frac{\mathrm{d}^2 w_0}{\mathrm{d}x^2}\right)\Bigg]^2\mathrm{d}x\end{aligned} \tag{3}$$

in which only the elastic part of the axial stress is considered. The virtual work of the viscous part of the Kelvin-Voigt stress is formulated as

$$\begin{aligned}\delta W_v = -\eta I\int_0^L\frac{\partial}{\partial t}\Bigg[&\frac{\partial^2 w}{\partial x^2} + \frac{\mathrm{d}w_0}{\mathrm{d}x}\frac{\mathrm{d}^2 w_0}{\mathrm{d}x^2}\frac{\partial w}{\partial x} + \frac{1}{2}\left(\frac{\mathrm{d}w_0}{\mathrm{d}x}\right)^2\frac{\partial^2 w}{\partial x^2} + \frac{\mathrm{d}w_0}{\mathrm{d}x}\frac{\partial w}{\partial x}\frac{\partial^2 w}{\partial x^2}\\ &+ \frac{1}{2}\left(\frac{\partial w}{\partial x}\right)^2\left(\frac{\partial^2 w}{\partial x^2} + \frac{\mathrm{d}^2 w_0}{\mathrm{d}x^2}\right)\Bigg]\delta\Bigg[\frac{\partial^2 w}{\partial x^2} + \frac{\mathrm{d}w_0}{\mathrm{d}x}\frac{\mathrm{d}^2 w_0}{\mathrm{d}x^2}\frac{\partial w}{\partial x}\\ &+ \frac{1}{2}\left(\frac{\mathrm{d}w_0}{\mathrm{d}x}\right)^2\frac{\partial^2 w}{\partial x^2} + \frac{\mathrm{d}w_0}{\mathrm{d}x}\frac{\partial w}{\partial x}\frac{\partial^2 w}{\partial x^2} + \frac{1}{2}\left(\frac{\partial w}{\partial x}\right)^2\left(\frac{\partial^2 w}{\partial x^2} + \frac{\mathrm{d}^2 w_0}{\mathrm{d}x^2}\right)\Bigg]\mathrm{d}x.\end{aligned} \tag{4}$$

Furthermore, the virtual work of the beam constraints, modelled as nonlinear springs, can be written as

$$\begin{aligned}\delta W_s = -\int_0^L \delta_D\left(x-x_s\right)\Big\{&\operatorname{sgn}\left(w+w_0\right)\mathrm{H}\left(\left|w+w_0\right|-g_0\right)\\ &\times\left[k_1\left(\left|w+w_0\right|-g_0\right)+k_3\left(\left|w+w_0\right|-g_0\right)^3\right]\Big\}\delta w\,\mathrm{d}x\end{aligned} \tag{5}$$

where δ_D, sgn, and H stand for the Dirac Delta, Sign, and Heaviside functions, respectively; || indicates the absolute value.

Substitution of Eqs. (2)-(5) into extended principle of Hamilton yields the nonlinear equation of motion of the constrained system as:

$$\begin{aligned}&-\rho A z_0\Omega^2\sin\left(\Omega t\right)+\rho A\frac{\partial}{\partial x}\left\{\left(\frac{\partial w}{\partial x}+\frac{\mathrm{d}w_0}{\mathrm{d}x}\right)\int_L^x\left(\int_0^x\left[\left(\frac{\partial w}{\partial x}+\frac{\mathrm{d}w_0}{\mathrm{d}x}\right)\frac{\partial^3 w}{\partial x\partial t^2}+\left(\frac{\partial^2 w}{\partial x\partial t}\right)^2\right]\mathrm{d}x\right)\mathrm{d}x\right\}\\
&+EI\frac{\partial}{\partial x}\left[\frac{\partial^3 w}{\partial x^3}+\left(\frac{\mathrm{d}w_0}{\mathrm{d}x}\right)^2\frac{\partial^3 w}{\partial x^3}+2\frac{\mathrm{d}w_0}{\mathrm{d}x}\frac{\mathrm{d}^2 w_0}{\mathrm{d}x^2}\frac{\partial^2 w}{\partial x^2}+\left(\frac{\mathrm{d}^2 w_0}{\mathrm{d}x^2}\right)^2\frac{\partial w}{\partial x}+\frac{\mathrm{d}w_0}{\mathrm{d}x}\frac{\mathrm{d}^3 w_0}{\mathrm{d}x^3}\frac{\partial w}{\partial x}\right.\\
&\qquad 2\frac{\mathrm{d}w_0}{\mathrm{d}x}\frac{\partial w}{\partial x}\frac{\partial^3 w}{\partial x^3}+\frac{1}{2}\frac{\mathrm{d}^3 w_0}{\mathrm{d}x^3}\left(\frac{\partial w}{\partial x}\right)^2+2\frac{\mathrm{d}^2 w_0}{\mathrm{d}x^2}\frac{\partial w}{\partial x}\frac{\partial^2 w}{\partial x^2}+\frac{\mathrm{d}w_0}{\mathrm{d}x}\left(\frac{\partial^2 w}{\partial x^2}\right)^2\\
&\qquad\left.+\frac{\partial w}{\partial x}\left(\frac{\partial^2 w}{\partial x^2}\right)^2+\frac{\partial^3 w}{\partial x^3}\left(\frac{\partial w}{\partial x}\right)^2\right]+\rho A\frac{\partial^2 w}{\partial t^2}\\
&+\eta I\frac{\partial}{\partial x}\left[\frac{\partial^4 w}{\partial x^3\partial t}+\left(\frac{\mathrm{d}w_0}{\mathrm{d}x}\right)^2\frac{\partial^4 w}{\partial x^3\partial t}+2\frac{\mathrm{d}w_0}{\mathrm{d}x}\frac{\mathrm{d}^2 w_0}{\mathrm{d}x^2}\frac{\partial^3 w}{\partial x^2\partial t}+\left(\frac{\mathrm{d}^2 w_0}{\mathrm{d}x^2}\right)^2\frac{\partial^2 w}{\partial x\partial t}\right.\\
&\qquad+\frac{\mathrm{d}w_0}{\mathrm{d}x}\frac{\mathrm{d}^3 w_0}{\mathrm{d}x^3}\frac{\partial^2 w}{\partial x\partial t}+2\frac{\mathrm{d}w_0}{\mathrm{d}x}\frac{\partial w}{\partial x}\frac{\partial^4 w}{\partial x^3\partial t}+2\frac{\mathrm{d}w_0}{\mathrm{d}x}\frac{\partial^2 w}{\partial x^2}\frac{\partial^3 w}{\partial x^2\partial t}+2\frac{\mathrm{d}^2 w_0}{\mathrm{d}x^2}\frac{\partial w}{\partial x}\frac{\partial^3 w}{\partial x^2\partial t}\\
&\qquad+\frac{\mathrm{d}w_0}{\mathrm{d}x}\frac{\partial^3 w}{\partial x^3}\frac{\partial^2 w}{\partial x\partial t}+\frac{\mathrm{d}^3 w_0}{\mathrm{d}x^3}\frac{\partial w}{\partial x}\frac{\partial^2 w}{\partial x\partial t}+2\frac{\mathrm{d}^2 w_0}{\mathrm{d}x^2}\frac{\partial^2 w}{\partial x^2}\frac{\partial^2 w}{\partial x\partial t}+\left(\frac{\partial^2 w}{\partial x^2}\right)^2\frac{\partial^2 w}{\partial x\partial t}\\
&\qquad\left.+2\frac{\partial w}{\partial x}\frac{\partial^2 w}{\partial x^2}\frac{\partial^3 w}{\partial x^2\partial t}+\left(\frac{\partial w}{\partial x}\right)^2\frac{\partial^4 w}{\partial x^3\partial t}+\frac{\partial w}{\partial x}\frac{\partial^3 w}{\partial x^3}\frac{\partial^2 w}{\partial x\partial t}\right]\\
&+\delta_D\left(x-x_s\right)\operatorname{sgn}\left(w+w_0\right)\mathrm{H}\left(\left|w+w_0\right|-g_0\right)\left[k_1\left(\left|w+w_0\right|-g_0\right)+k_3\left(\left|w+w_0\right|-g_0\right)^3\right]=0\end{aligned} \tag{6}$$

This equation is then transformed into the following dimensionless form

$$
\begin{aligned}
&-z_0\Omega_b^2\sin\left(\Omega_b t\right)+\frac{\partial}{\partial x}\left\{\left(\frac{\partial w}{\partial x}+\frac{\mathrm{d}w_0}{\mathrm{d}x}\right)\int_1^x\left(\int_0^x\left[\left(\frac{\partial w}{\partial x}+\frac{\mathrm{d}w_0}{\mathrm{d}x}\right)\frac{\partial^3 w}{\partial x\partial t^2}+\left(\frac{\partial^2 w}{\partial x\partial t}\right)^2\right]\mathrm{d}x\right)\mathrm{d}x\right\}\\
&+\frac{\partial^2 w}{\partial t^2}+\frac{\partial}{\partial x}\left[\frac{\partial^3 w}{\partial x^3}+\left(\frac{\mathrm{d}w_0}{\mathrm{d}x}\right)^2\frac{\partial^3 w}{\partial x^3}+2\frac{\mathrm{d}w_0}{\mathrm{d}x}\frac{\mathrm{d}^2 w_0}{\mathrm{d}x^2}\frac{\partial^2 w}{\partial x^2}+\left(\frac{\mathrm{d}^2 w_0}{\mathrm{d}x^2}\right)^2\frac{\partial w}{\partial x}+\frac{\mathrm{d}w_0}{\mathrm{d}x}\frac{\mathrm{d}^3 w_0}{\mathrm{d}x^3}\frac{\partial w}{\partial x}\right.\\
&\qquad 2\frac{\mathrm{d}w_0}{\mathrm{d}x}\frac{\partial w}{\partial x}\frac{\partial^3 w}{\partial x^3}+\frac{1}{2}\frac{\mathrm{d}^3 w_0}{\mathrm{d}x^3}\left(\frac{\partial w}{\partial x}\right)^2+2\frac{\mathrm{d}^2 w_0}{\mathrm{d}x^2}\frac{\partial w}{\partial x}\frac{\partial^2 w}{\partial x^2}+\frac{\mathrm{d}w_0}{\mathrm{d}x}\left(\frac{\partial^2 w}{\partial x^2}\right)^2\\
&\qquad \left.+\frac{\partial w}{\partial x}\left(\frac{\partial^2 w}{\partial x^2}\right)^2+\frac{\partial^3 w}{\partial x^3}\left(\frac{\partial w}{\partial x}\right)^2\right]\\
&+\eta_d\frac{\partial}{\partial x}\left[\frac{\partial^4 w}{\partial x^3\partial t}+\left(\frac{\mathrm{d}w_0}{\mathrm{d}x}\right)^2\frac{\partial^4 w}{\partial x^3\partial t}+2\frac{\mathrm{d}w_0}{\mathrm{d}x}\frac{\mathrm{d}^2 w_0}{\mathrm{d}x^2}\frac{\partial^3 w}{\partial x^2\partial t}+\left(\frac{\mathrm{d}^2 w_0}{\mathrm{d}x^2}\right)^2\frac{\partial^2 w}{\partial x\partial t}\right.\\
&\qquad +\frac{\mathrm{d}w_0}{\mathrm{d}x}\frac{\mathrm{d}^3 w_0}{\mathrm{d}x^3}\frac{\partial^2 w}{\partial x\partial t}+2\frac{\mathrm{d}w_0}{\mathrm{d}x}\frac{\partial w}{\partial x}\frac{\partial^4 w}{\partial x^3\partial t}+2\frac{\mathrm{d}w_0}{\mathrm{d}x}\frac{\partial^2 w}{\partial x^2}\frac{\partial^3 w}{\partial x^2\partial t}+2\frac{\mathrm{d}^2 w_0}{\mathrm{d}x^2}\frac{\partial w}{\partial x}\frac{\partial^3 w}{\partial x^2\partial t}\\
&\qquad +\frac{\mathrm{d}w_0}{\mathrm{d}x}\frac{\partial^3 w}{\partial x^3}\frac{\partial^2 w}{\partial x\partial t}+\frac{\mathrm{d}^3 w_0}{\mathrm{d}x^3}\frac{\partial w}{\partial x}\frac{\partial^2 w}{\partial x\partial t}+2\frac{\mathrm{d}^2 w_0}{\mathrm{d}x^2}\frac{\partial^2 w}{\partial x^2}\frac{\partial^2 w}{\partial x\partial t}+\left(\frac{\partial^2 w}{\partial x^2}\right)^2\frac{\partial^2 w}{\partial x\partial t}\\
&\qquad \left.+2\frac{\partial w}{\partial x}\frac{\partial^2 w}{\partial x^2}\frac{\partial^3 w}{\partial x^2\partial t}+\left(\frac{\partial w}{\partial x}\right)^2\frac{\partial^4 w}{\partial x^3\partial t}+\frac{\partial w}{\partial x}\frac{\partial^3 w}{\partial x^3}\frac{\partial^2 w}{\partial x\partial t}\right]\\
&+\delta_D\left(x-x_s\right)\mathrm{sgn}\left(w+w_0\right)\mathrm{H}\left(\left|w+w_0\right|-g_0\right)\left[K_1\left(\left|w+w_0\right|-g_0\right)+K_3\left(\left|w+w_0\right|-g_0\right)^3\right]=0
\end{aligned}
\tag{7}
$$

using the following dimensionless parameters

$$
\begin{aligned}
&t^*=\frac{t}{\tau},\ \eta_d=\frac{\eta}{E\tau},\ w_0^*=\frac{w_0}{L},\ w^*=\frac{w}{L},\ x^*=\frac{x}{L},\ x_s^*=\frac{x_s}{L},\\
&z_0^*=\frac{z_0}{L},\ \Omega_b=\Omega\tau,\ g_0^*=\frac{g_0}{L},\ K_1=\frac{k_1L^3}{EI},\ K_3=\frac{k_3L^5}{EI},
\end{aligned}
\tag{8}
$$

where $\tau=L^2\sqrt{\rho A/(EI)}$. In Eq. (7), the asterisk notation is dropped for convenience.

In what follows, a modal discretisation procedure based on the Galerkin approach is utilised to reduce the nonlinear nondimensional equation of motion into a set of discretised equations of ordinary differential type. In the modal decomposition technique, a finite number of modes (generalised coordinates) are considered to describe the motion of the system. These generalised coordinates, denoted by $w_r(t)$, are multiplied by proper spatial

trial functions, denoted by $\Lambda_r(x)$. Hence, the transverse motion, *w*, is expanded as a summation of $\Lambda_r(x)w_r(t)$ for *r* in the range 1, 2, …, *Q*. Additionally, the initial curvature of the beam, w_0, is represented by $A_0\Lambda_1(x)$, with A_0 being the initial curvature amplitude. Λ_r is given by:

$$\Lambda_r(x)=\left[\cosh\left(\xi_r x\right)-\alpha_r\sinh\left(\xi_r x\right)\right]-\left[\cos\left(\xi_r x\right)-\alpha_r\sin\left(\xi_r x\right)\right], \tag{9}$$

in which $\alpha_r=\left[\cos\left(\xi_r\right)-\cosh\left(\xi_r\right)\right]/\left[\sin\left(\xi_r\right)-\sinh\left(\xi_r\right)\right]$; ξ_r is obtained by calculating the *r*th root of $\cos\left(\xi\right)\cosh\left(\xi\right)-1=0$.

Application of the method of Galerkin gives

$$\sum_{l=1}^{Q}\sum_{m=1}^{Q}\sum_{n=1}^{Q}\left[\int_0^1\left(\begin{array}{l}\left(\Lambda_l'+\Lambda_1'\right)\Lambda_k\int_0^x\left(\Lambda_m'+\Lambda_1'\right)\Lambda_n'\,\mathrm{d}x\\ +\left(\Lambda_l''+\Lambda_1''\right)\Lambda_k\int_1^x\int_0^x\left(\Lambda_1'+\Lambda_m'\right)\Lambda_n'\,\mathrm{d}x\,\mathrm{d}x\end{array}\right)\mathrm{d}x\right]w_l w_m\ddot{w}_n$$

$$+\sum_{l=1}^{Q}\sum_{m=1}^{Q}\sum_{n=1}^{Q}\left[\int_0^1\left(\left(\Lambda_l''+\Lambda_1''\right)\Lambda_k\int_1^x\int_0^x\Lambda_m'\Lambda_n'\,\mathrm{d}x\,\mathrm{d}x+\left(\Lambda_l'+\Lambda_1'\right)\Lambda_k\int_0^x\Lambda_m'\Lambda_n'\,\mathrm{d}x\right)\mathrm{d}x\right]w_l\dot{w}_m\dot{w}_n$$

$$+\sum_{l=1}^{Q}\left(\int_0^1\Lambda_k\Lambda_l\,\mathrm{d}x\right)\ddot{w}_l+\sum_{l=1}^{Q}\left(\int_0^1\Lambda_k\Lambda_l''''\,\mathrm{d}x\right)\left(w_l+\eta_d\dot{w}_l\right)-\int_0^1\Lambda_k z_0\Omega_b^2\sin\left(\Omega_b t\right)\mathrm{d}x$$

$$+\sum_{l=1}^{Q}\sum_{m=1}^{Q}\sum_{n=1}^{Q}\left[\int_0^1\left(\Lambda_k\Lambda_l''\Lambda_m''\Lambda_n''+4\Lambda_k\Lambda_l'\Lambda_m''\Lambda_n'''+\Lambda_k\Lambda_l'\Lambda_m'\Lambda_n''''\right)\mathrm{d}x\right]w_l w_m w_n$$

$$+\sum_{l=1}^{Q}\sum_{m=1}^{Q}\left[\int_0^1\left(\begin{array}{l}\frac{1}{2}\Lambda_k\Lambda_l'\Lambda_m'\Lambda_1''''+3\Lambda_k\Lambda_l''\Lambda_m''\Lambda_1''+2\Lambda_k\Lambda_1'\Lambda_l'\Lambda_m''''+4\Lambda_k\Lambda_l'\Lambda_1''\Lambda_m'''\\ +4\Lambda_k\Lambda_1'\Lambda_l''\Lambda_m'''+3\Lambda_k\Lambda_l'\Lambda_m''\Lambda_1'''\end{array}\right)\mathrm{d}x\right]A_0 w_l w_m$$

$$+\sum_{l=1}^{Q}\left[\int_0^1\left(\begin{array}{l}\Lambda_k\Lambda_l'\Lambda_1'\Lambda_1''''+3\Lambda_k\Lambda_l''\Lambda_1''\Lambda_1''+\Lambda_k\Lambda_1'\Lambda_1'\Lambda_l''''+3\Lambda_k\Lambda_l'\Lambda_1''\Lambda_1'''\\ +4\Lambda_k\Lambda_1'\Lambda_1''\Lambda_m'''+3\Lambda_k\Lambda_1'\Lambda_l''\Lambda_1'''\end{array}\right)\mathrm{d}x\right]A_0^2 w_l$$

$$+\eta_d\sum_{l=1}^{Q}\sum_{m=1}^{Q}\sum_{n=1}^{Q}\left[\int_0^1\left(\begin{array}{l}\Lambda_k\Lambda_l'\Lambda_m'\Lambda_n''''+\Lambda_k\Lambda_l'\Lambda_m''''\Lambda_n'+4\Lambda_k\Lambda_l'\Lambda_m''\Lambda_n'''\\ +3\Lambda_k\Lambda_l'''\Lambda_m''\Lambda_n'+3\Lambda_k\Lambda_l'''\Lambda_m'\Lambda_n''+3\Lambda_k\Lambda_l''\Lambda_m''\Lambda_n''\end{array}\right)\mathrm{d}x\right]w_l w_m\dot{w}_n$$

$$+\eta_d\sum_{l=1}^{Q}\sum_{m=1}^{Q}\left[\int_0^1\left(\begin{array}{l}2\Lambda_k\Lambda_1'\Lambda_l'\Lambda_m''''+4\Lambda_k\Lambda_l'\Lambda_1''\Lambda_m'''+4\Lambda_k\Lambda_1'\Lambda_l''\Lambda_m'''+3\Lambda_k\Lambda_1'''\Lambda_l''\Lambda_m'\\ +\Lambda_k\Lambda_1'\Lambda_l''''\Lambda_m'+3\Lambda_k\Lambda_l'''\Lambda_1'\Lambda_m''+6\Lambda_k\Lambda_1''\Lambda_l''\Lambda_m''\\ +\Lambda_k\Lambda_l'\Lambda_1''''\Lambda_m'+3\Lambda_k\Lambda_l'''\Lambda_1''\Lambda_m'+3\Lambda_k\Lambda_1'''\Lambda_l'\Lambda_m''\end{array}\right)\mathrm{d}x\right]A_0 w_l\dot{w}_m$$

$$+\eta_d\sum_{l=1}^{Q}\left[\int_0^1\left(\begin{array}{l}\Lambda_k\Lambda_1'\Lambda_1'\Lambda_l''''+3\Lambda_k\Lambda_1'''\Lambda_1'\Lambda_l''+4\Lambda_k\Lambda_1'\Lambda_1''\Lambda_l'''\\ +3\Lambda_k\Lambda_1''\Lambda_1''\Lambda_l''+\Lambda_k\Lambda_1'\Lambda_1''''\Lambda_l'+3\Lambda_k\Lambda_1'''\Lambda_1''\Lambda_l'\end{array}\right)\mathrm{d}x\right]A_0^2\dot{w}_l$$

$$+\int_0^1 \Lambda_k \left\{ \delta_D(x-x_s) H\left(\left| A_0\Lambda_1 + \sum_{l=1}^{Q} \Lambda_l w_l \right| - g_0 \right) \operatorname{sgn}\left(A_0\Lambda_1 + \sum_{l=1}^{Q} \Lambda_l w_l \right) \right.$$
$$\left. \times \left[K_1 \left(\left| A_0\Lambda_1 + \sum_{l=1}^{Q} \Lambda_l w_l \right| - g_0 \right) + K_3 \left(\left| A_0\Lambda_1 + \sum_{l=1}^{Q} \Lambda_l w_l \right| - g_0 \right)^3 \right] \right\} \mathrm{d}x = 0, \quad (10)$$

$k = 1, 2, ..., Q.$

In this study, Q is set to 8, i.e. 8 transverse vibration modes are kept in the transverse displacement series expansion. This results in an 8-degree-of-freedom (DOF) discretised model consisting of various sources of nonlinearity including: geometric nonlinearity, inertial nonlinearity, damping nonlinearity, and piecewise nonlinearity. The presence of all these nonlinearities together with the large number of retained modes increases the complexity and the computational costs significantly. A well-optimised continuation [36, 37] code is developed to handle various types of nonlinearities. The numerical results are obtained for various cases and discussed in detail in the next section.

3. Numerical results for nonlinear dynamics of unconstrained system

Before analysing the nonlinear constrained vibration dynamics of the system, it would be interesting to analyse the initially curved beam dynamical behaviour without any constraints for comparison purposes.

3.1 Verification of the developed model and numerical simulations

To check the proposed model's accuracy as well as the reliability of the employed numerical technique, a natural frequency analysis and a nonlinear static analysis are conducted employing the developed model and compared to the results obtained through

nonlinear finite element analysis using Abaqus. For this comparison, a beam of h=0.5 mm, L/h=200, and b/h=4 is considered.

For the natural frequency comparison, the calculated fundamental natural frequency using FEA is converted to rad/s and then made dimensionless through multiplying by $\tau = L^2\sqrt{\rho A/(EI)}$. The comparison is shown in Fig. 2, showing that the predictions of the initially curved beam model developed in this study are very close to those obtained using FEA.

The nonlinear deformation of the initially curved beam calculated via the present study is compared to that obtained using FEA and plotted in Fig. 3. For this case, it is assumed that a point force f is exerted to the beam midpoint in the negative transverse direction; A_0 is set to 0.05. The axial axis in Fig. 3 shows the dimensionless force (i.e. $F = fL^2/(EI)$) while the vertical axis shows the dimensionless transverse displacement at beam midpoint. The results are shown for (a) transverse displacement at beam midpoint and (b) longitudinal displacement at beam movable tip. As seen, the nonlinear static displacements predicted by the model developed in this study are very close to those obtained via FEA. Figure 4 shows the contour plots of the initial curved beam as it undergoes static deformation due to applied midpoint force. The comparison of the predicted deformed state of the initially curved beam via the proposed model and FEA is shown in Fig. 5. As seen, the deformed beam profiles obtained by the two models are almost the same. Hence, the developed model is checked and verified for both linear natural frequency calculations and nonlinear static deformation.

3.2 Nonlinear unconstrained dynamics

Figure 6 shows the amplitude-frequency curves of the unconstrained initially curved beam under base excitation in the primary resonance region, with ω_1 denoting the fundamental natural frequency; η_d=0.00035. Sub-figure (a) illustrates the transverse displacement at beam mid-point while sub-figure (b) shows the longitudinal displacement at the axially movable tip. It is seen that the initially curved configuration of the beam results in a complex resonance response with strong internal resonances and modal interactions. More specifically, for the selected system parameters, the second natural frequency of the transverse motion is around three times the first natural frequency, giving rise to a three-to-one internal resonance; the energy transfer between the first two modes can be seen by comparing sub-figures (c) and (d). Furthermore, the system displays multiple jumps and snap-through motions moving between different stable solution branches. Additionally, it is interesting to note that the initially curved beam display quasiperiodic motion for a range of base excitation frequency, shown by dotted lines in the figures. The vibrating beam response in one period of oscillation is depicted in Fig. 7 for two different excitation frequencies. It is shown that the axial movement of the clamped end is very large and comparable to maximum transverse displacement.

The amplitude-frequency plots for different magnitudes of the initial curvature are obtained and plotted in Fig. 8. For the values of initial curvature examined here, the maximum transverse and longitudinal displacements correspond to the case with A_0=0.10. As seen, increasing the initial curvature amplitude shifts the primary resonance region to smaller excitation frequencies, indicating reduced fundamental natural frequency. It is worth noting that for beams with immovable boundaries, i.e. extensible beams, the

presence of imperfection increases the natural frequency. The difference in the behaviour is due to inextensibility of the system in the present study. In other words, due to inextensibility of the centreline, the natural frequency decreases with increasing imperfection amplitude.

4. Numerical results for nonlinear dynamics of constrained system

This section investigates the nonlinear dynamics of the constrained beam. In particular, the elastic constraints are assumed to be present at both sides of the in the transverse direction. For all cases, the elastic constraints are positioned at a distance x_s=0.2 from the immovable clamped end. Additionally, η_d=0.00035 throughout this section.

The forced vibration response of the constrained beam in the region of primary resonance is illustrated in Fig. 9 for *w* and *u* motions. The system parameters are set to: g_0= 0.05, K_1=2.0×10^3 K_3=2.0×10^6, and z_0=0.002. It is seen that due to the presence of motion-limiting elastic constraints, the resonance force vibration response becomes very complex. In particular, the constrained system displays a mixed hardening softening behaviour as well as different saddle-node and torus bifurcation points. Torus bifurcations give rise to quasiperiodic solution branches, shown by dotted lines in the figures. The figure shows that as the impact between the beam and the constraints is characterised by a sudden change of slope in the curves and change of nonlinear response from softening to hardening type. It is seen that for the frequency range shown in the figures, multiple stable periodic attractors (shown by solid lines) and stable quasiperiodic attractors (shown by dotted lines) are present. The constrained beam could be oscillating on any of these attractors depending on the initial condition and external disturbances. The unstable attractors are shown by dashed

lines. To better illustrate the motion that the constrained beam undergo in one period of oscillation, Fig. 10 is constructed. This figure shows the constrained beam oscillation at Ω_b/ω_1 = 0.9764, i.e. at peak oscillation amplitude, in one period of oscillation. It is seen that the presence of an initial curvature results in asymmetric oscillation.

The frequency-amplitude curves of a constrained beam similar to that of Fig. 9, but with larger base-excitation amplitude, are shown in Fig. 11. More specifically, all the system parameters remain unchanged compared to Fig. 9, except for z_0, which is set to 0.006 in this figure. As seen, as a result of increased base excitation amplitude (compared to the system of Fig. 9) the response changes significantly. In this case, two period-doubling bifurcations occur in the vicinity of peak oscillation amplitude giving rise to a new bifurcated solution branch (see the magnified section in sub-figure (a)). The constrained beam displays quasiperiodic motion for a portion of this bifurcation solution branch and periodic motion for the rest. In order to compare dynamical characteristics of the constrained beam before and after the occurrence of the periodic-doubling bifurcation, Figs. 12 and 13 are constructed illustrating the time histories and plots of phase-plane of the transverse and longitudinal motions at Ω_b/ω_1=0.9351, i.e. on the stable branch before period-doubling bifurcation, and Ω_b/ω_1=0.9420, i.e. the stable branch of the bifurcated solution.

The effect of the amplitude of the initial curvature on dynamics characteristics of the constrained system is depicted in Fig. 14. The system parameters are set to: z_0=0.003, x_s=0.2, g_0=0.08, K_1=2.0×10^3, and K_3=2.0×10^6. Since the gap width is fixed for all cases, increasing the initial curvature amplitude reduces the clearance between the beam and the upper constraint and increases that between the beam and lower constraint. Hence, as the initial curvature amplitude is increased, the change in the response slope occurs at smaller

oscillation amplitudes. Additionally, the hardening behaviour is stronger when the initial curvature amplitude is set to larger values.

One of the important parameters of the constrained system is the initial gap width g_0. It should be mentioned here again that in this study, the gap width is defined as the distance between the elastic constraints and the axial axis (see Fig. 1). The effect of the gap width on nonlinear vibration response of the constrained beam is depicted in Fig. 15. The system parameters are selected as: z_0=0.003, A_0=0.05, x_s=0.2, K_1=2.0×10^3, and K_3=2.0×10^6. It is seen that forced dynamic characteristics of the constrained beam are affected significantly with slight change in the gap width. More specifically, as the gap is decreased, the impact between beam and constraints occur at smaller motion amplitudes. This causes the sharp change of response slope to occur at smaller oscillation magnitudes. Additionally, due to decreased gap width, the response amplitude is decreased and the induced nonlinear hardening behaviour is strengthened.

The effect of the linear spring coefficient of the elastic constraint on resonant dynamic characteristics of the constrained beam is shown in Fig. 16. For this case, z_0=0.002, A_0=0.05, x_s=0.2, g_0=0.06, and K_3=2.0×10^6. The figure show that due to increased K_1, the oscillation amplitude decreases significantly. Additionally, it is observed that the change in the response slope, due to contact initiation between the beam and the constraints, becomes sharper as the linear spring coefficient is increased. Figure 17 shows the effect of the nonlinear spring coefficient of the elastic constraint on resonant forced response. As seen, the nonlinear hardening behaviour is strengthened as a result of increased K_3.

Figure 18 shows a comparison of the resonant responses of three systems: a system with no constraints, and two constrained systems with different stiffness coefficients. For

the “elastic constraints” case K_1=2.0×10^3 and K_2=2.0×10^6, while for “rigid constraints” case K_1=10.0×10^3 and K_2=200.0×10^6. It is very interesting to note that the constrained system with elastic constraints undergoes larger-amplitude oscillation compared to the unconstrained system. Moreover, it is seen that as the spring coefficients of the constraints are set to large values, to simulate rigid constraints, the transverse amplitude at x= 0.2, i.e. where the constraints are located, increases only slightly after hitting the constraints. The oscillations of these three systems at peak amplitude are illustrated in Fig. 19.

5. Concluding remarks

The nonlinear dynamics of an initially curved constrained beam has been studied numerically. The beam is considered to have an initial curvature. The fully nonlinear model of the constrained beam is developed taking into account geometric, inertial, damping, and piecewise nonlinearities. The Kelvin-Voigt model is utilised along with Euler-Bernoulli beam theory to derive the nonlinear motion equation while assuming inextensible centreline due to one end being axially movable. The Galerkin modal discretisation procedure is used to derive a discretised model of the constrained system.

Numerical simulations were conducted for both unconstrained and constrained systems. The nonlinear dynamics of unconstrained system showed that the presence of initial curvature gives rise strong modal interactions as well as quasiperiodic motion. Additionally, it was shown that increasing the initial curvature amplitude results in decreased natural frequency and hence resonant region being shifted to the left on frequency axis.

The constrained nonlinear dynamic analysis revealed that the presence of elastic constraints renders the motion much more complex and gives rise to many bifurcation points and many stable and unstable attractors. It was shown that at larger base excitation amplitudes, period-doubling bifurcation occurs resulting in a new bifurcation solution branch with both quasiperiodic and periodic attractors. The effect of various parameters was examined and it was shown that: decreasing the gap width reduces the vibration amplitude and causes the slope-change to occur at smaller oscillation amplitudes; increasing the linear spring coefficient results in increased change of slope at point of contact while increasing the nonlinear spring coefficient strengthens the hardening behaviour after

contact; increasing the amplitude of the initial curvature causes the contact to initiate at smaller oscillation amplitudes and results in a wider hardening response range after initiation of contact.

Appendix A. Analysis of Convergence

An analysis of convergence is performed to justify selection of 8 modes in this study. To this end, the amplitude-frequency diagram of the constrained system of Fig. 9 is reconstructed for different discretised models of the system namely, a 2-degree-of-freedom (2-DOF), 4-DOF, 8-DOF, and 10-DOF systems. As seen, the 2-DOF model gives wrong results. The predictions of the 4-DOF model are closer to converged results, however is not yet fully converged. The 8-DOF model predicts the same resonance amplitudes as the 10-DOF model indicating convergence. This convergence analysis shows that an 8-DOF model is accurate enough and ensures converged results.

References

[1] S. Panda, B. Singh, Nonlinear free vibration of spherical shell panel using higher order shear deformation theory–a finite element approach, International Journal of Pressure Vessels and Piping, 86 (2009) 373-383.
[2] W. Zhang, Y. Hao, J. Yang, Nonlinear dynamics of FGM circular cylindrical shell with clamped–clamped edges, Composite Structures, 94 (2012) 1075-1086.
[3] V.K. Singh, S.K. Panda, Nonlinear free vibration analysis of single/doubly curved composite shallow shell panels, Thin-Walled Structures, 85 (2014) 341-349.
[4] Y. Hao, W. Zhang, J. Yang, Nonlinear oscillation of a cantilever FGM rectangular plate based on third-order plate theory and asymptotic perturbation method, Composites Part B: Engineering, 42 (2011) 402-413.
[5] W. Zhang, J. Yang, Y. Hao, Chaotic vibrations of an orthotropic FGM rectangular plate based on third-order shear deformation theory, Nonlinear Dynamics, 59 (2010) 619-660.
[6] Y. Hao, L. Chen, W. Zhang, J. Lei, Nonlinear oscillations, bifurcations and chaos of functionally graded materials plate, Journal of Sound and Vibration, 312 (2008) 862-892.
[7] W. Zhang, D. Wang, M. Yao, Using Fourier differential quadrature method to analyze transverse nonlinear vibrations of an axially accelerating viscoelastic beam, Nonlinear Dynamics, 78 (2014) 839-856.
[8] X.-D. Yang, W. Zhang, Nonlinear dynamics of axially moving beam with coupled longitudinal–transversal vibrations, Nonlinear Dynamics, 78 (2014) 2547-2556.
[9] W. Zhang, Chaotic motion and its control for nonlinear nonplanar oscillations of a parametrically excited cantilever beam, Chaos, Solitons & Fractals, 26 (2005) 731-745.
[10] W. Zhang, F. Wang, M. Yao, Global bifurcations and chaotic dynamics in nonlinear nonplanar oscillations of a parametrically excited cantilever beam, Nonlinear Dynamics, 40 (2005) 251-279.
[11] H. Tang, L. Li, Y. Hu, W. Meng, K. Duan, Vibration of nonlocal strain gradient beams incorporating Poisson's ratio and thickness effects, Thin-Walled Structures, 137 (2019) 377-391.
[12] M. Javani, Y. Kiani, M.R. Eslami, Free vibration of arbitrary thick FGM deep arches using unconstrained higher-order shear deformation theory, Thin-Walled Structures, 136 (2019) 258-266.
[13] C.C. Hong, GDQ computation for thermal vibration of thick FGM plates by using fully homogeneous equation and TSDT, Thin-Walled Structures, 135 (2019) 78-88.
[14] N.L. Nguyen, G.W. Jang, S. Choi, J. Kim, Y.Y. Kim, Analysis of thin-walled beam-shell structures for concept modeling based on higher-order beam theory, Computers and Structures, 195 (2018) 16-33.
[15] X. Li, C.C. Du, Y.H. Li, Parametric instability of a functionally graded cylindrical thin shell subjected to both axial disturbance and thermal environment, Thin-Walled Structures, 123 (2018) 25-35.
[16] R. Bahaadini, A.R. Saidi, Stability analysis of thin-walled spinning reinforced pipes conveying fluid in thermal environment, European Journal of Mechanics, A/Solids, 72 (2018) 298-309.
[17] A.R. Ashoori, S.A. Sadough Vanini, Nonlinear bending, postbuckling and snap-through of circular size-dependent functionally graded piezoelectric plates, Thin-Walled Structures, 111 (2017) 19-28.

[18] N.-I. Kim, J. Lee, Coupled vibration characteristics of shear flexible thin-walled functionally graded sandwich I-beams, Composites Part B: Engineering, 110 (2017) 229-247.
[19] K. Mehar, S.K. Panda, T.R. Mahapatra, Large deformation bending responses of nanotube-reinforced polymer composite panel structure: Numerical and experimental analyses, Proceedings of the Institution of Mechanical Engineers, Part G: Journal of Aerospace Engineering, 233 (2019) 1695-1704.
[20] K. Mehar, S.K. Panda, Theoretical deflection analysis of multi-walled carbon nanotube reinforced sandwich panel and experimental verification, Composites Part B: Engineering, 167 (2019) 317-328.
[21] K. Mehar, T.R. Mahapatra, S.K. Panda, P.V. Katariya, U.K. Tompe, Finite-element solution to nonlocal elasticity and scale effect on frequency behavior of shear deformable nanoplate structure, Journal of Engineering Mechanics, 144 (2018) 04018094.
[22] F.C. Moon, S.W. Shaw, Chaotic vibrations of a beam with non-linear boundary conditions, International Journal of Non-Linear Mechanics, 18 (1983) 465-477.
[23] S.W. Shaw, R.H. Rand, The transition to chaos in a simple mechanical system, International Journal of Non-Linear Mechanics, 24 (1989) 41-56.
[24] G.X. Li, R.H. Rand, F.C. Moon, Bifurcations and chaos in a forced zero-stiffness impact oscillator, International Journal of Non-Linear Mechanics, 25 (1990) 417-432.
[25] S. Natsiavas, On the dynamics of oscillators with bi-linear damping and stiffness, International Journal of Non-Linear Mechanics, 25 (1990) 535-554.
[26] M.M. Nigm, A.A. Shabana, Effect of an impact damper on a multi-degree of freedom system, Journal of Sound and Vibration, 89 (1983) 541-557.
[27] Y.S. Choi, S.T. Noah, Forced periodic vibration of unsymmetric piecewise-linear systems, Journal of Sound and Vibration, 121 (1988) 117-126.
[28] V.N. Pilipchuk, Strongly nonlinear vibrations of damped oscillators with two nonsmooth limits, Journal of Sound and Vibration, 302 (2007) 398-402.
[29] L. Charroyer, O. Chiello, J.J. Sinou, Self-excited vibrations of a non-smooth contact dynamical system with planar friction based on the shooting method, International Journal of Mechanical Sciences, 144 (2018) 90-101.
[30] U. Björkenstam, Impact vibration of a bar, International Journal of Mechanical Sciences, 19 (1977) 471-481.
[31] S. Masri, Y. Mariamy, J. Anderson, Dynamic response of a beam with a geometric nonlinearity, Journal of Applied Mechanics, 48 (1981) 404-410.
[32] P. Metallidis, S. Natsiavas, Vibration of a continuous system with clearance and motion constraints, International Journal of Non-Linear Mechanics, 35 (2000) 675-690.
[33] C. Issanchou, S. Bilbao, J.-L. Le Carrou, C. Touzé, O. Doaré, A modal-based approach to the nonlinear vibration of strings against a unilateral obstacle: Simulations and experiments in the pointwise case, Journal of Sound and Vibration, 393 (2017) 229-251.
[34] H. Liu, C. Lee, T. Kobayashi, C.J. Tay, C. Quan, Piezoelectric MEMS-based wideband energy harvesting systems using a frequency-up-conversion cantilever stopper, Sensors and Actuators A: Physical, 186 (2012) 242-248.
[35] M.S.M. Soliman, E.M. Abdel-Rahman, E.F. El-Saadany, R.R. Mansour, A wideband vibration-based energy harvester, Journal of Micromechanics and Microengineering, 18 (2008) 115021.
[36] H.D. Mittelmann, A pseudo-arclength continuation method for nonlinear eigenvalue problems, SIAM journal on numerical analysis, 23 (1986) 1007-1016.

[37] E.L. Allgower, K. Georg, Introduction to Numerical Continuation Methods, Society for Industrial and Applied Mathematics, 2003.

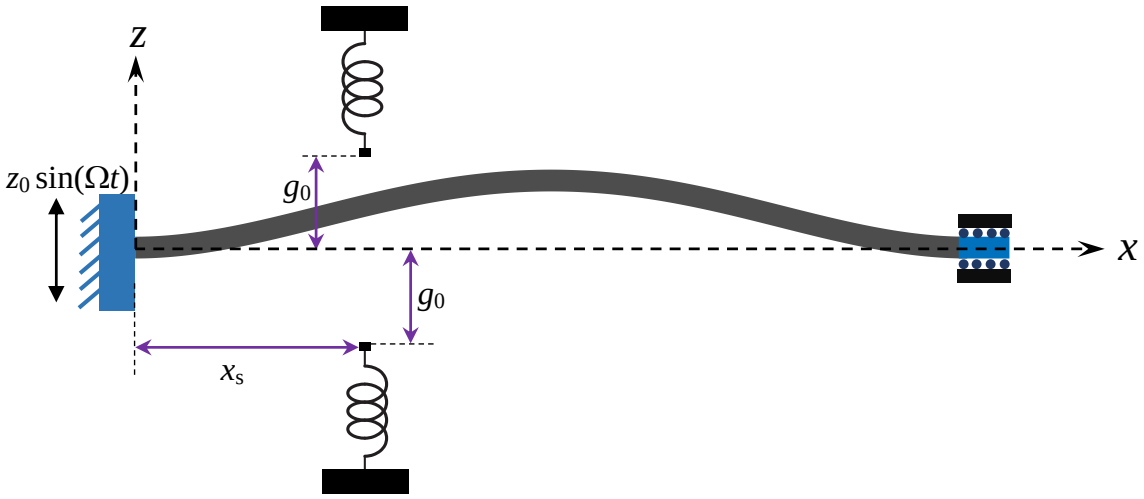

Fig. 1. Schematic of the doubly clamped constrained beam with one axially-movable end. The whole system is under base excitation.

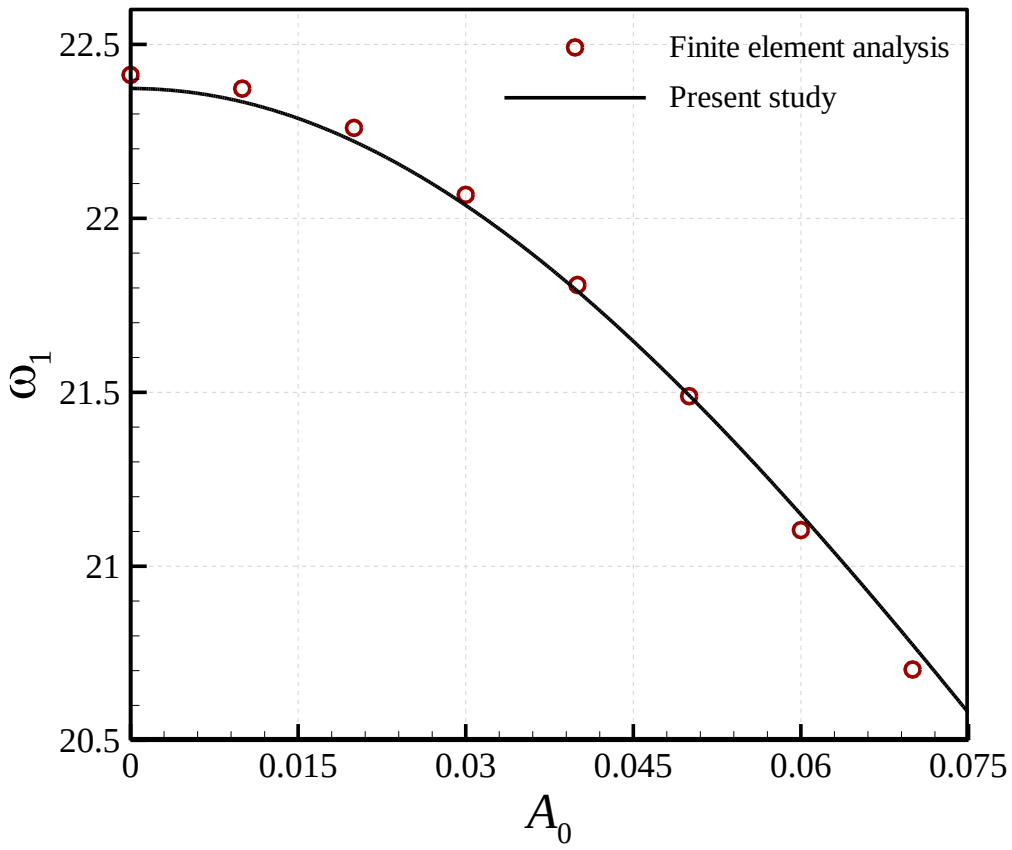

Fig.2. Fundamental dimensionless natural frequency of the initially curved beam obtained using the proposed model and finite element analysis.

(a)

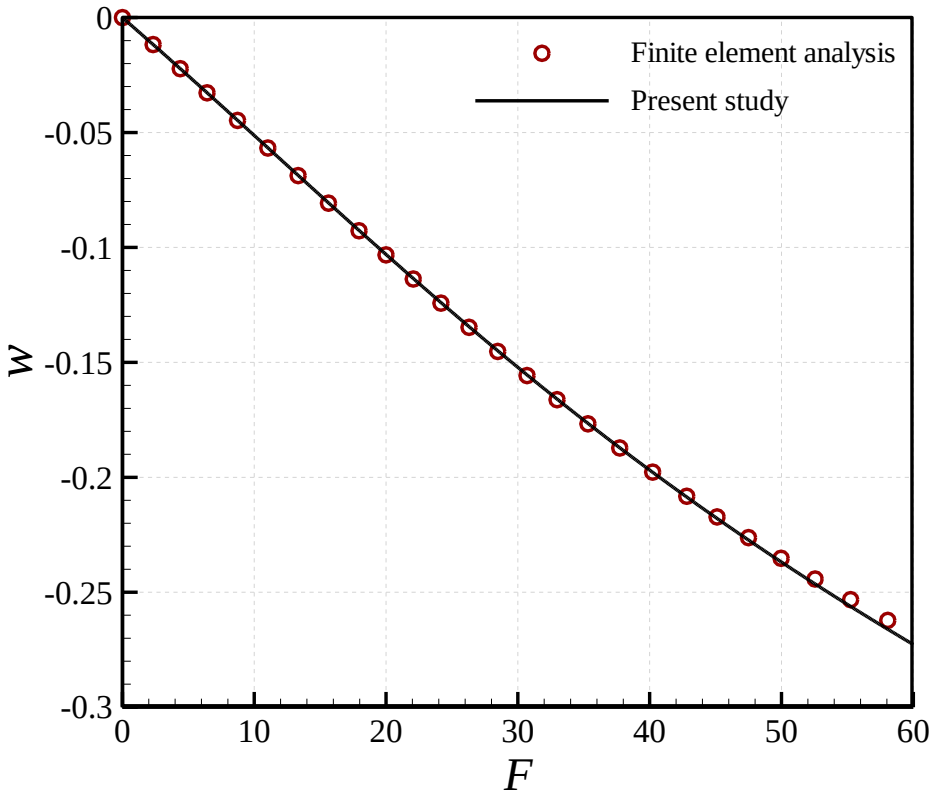

(b)

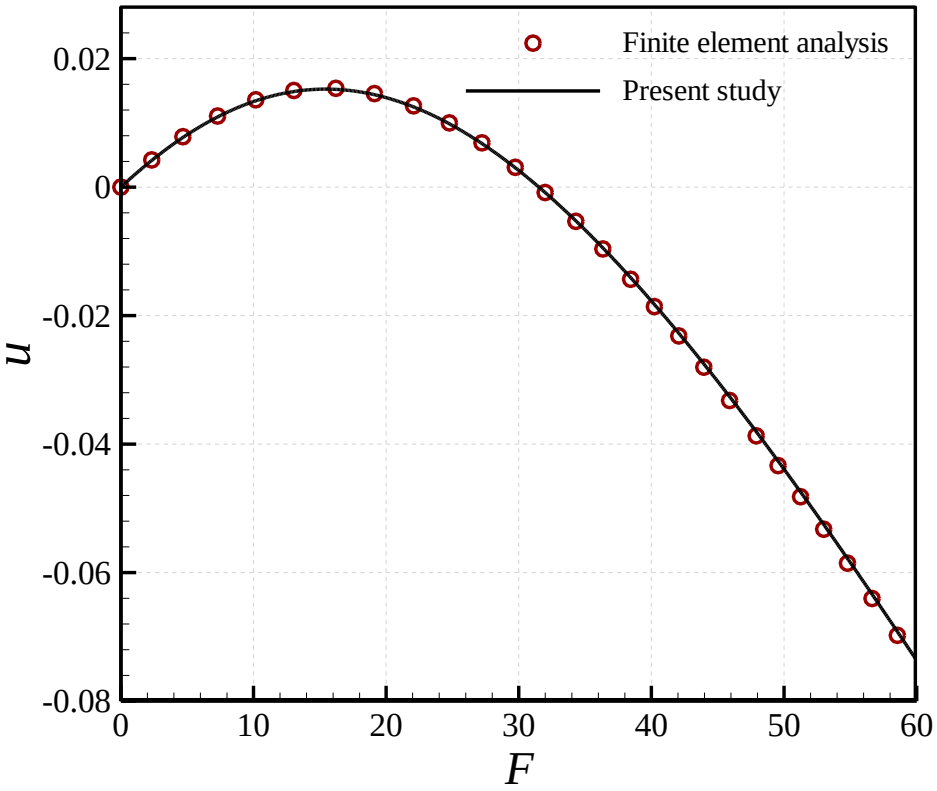

Fig.3. Nonlinear deformation of the initially curved beam calculated using the proposed model and finite element analysis; (a) w at x=0.5; (b) u at x=1. A_0=0.05.

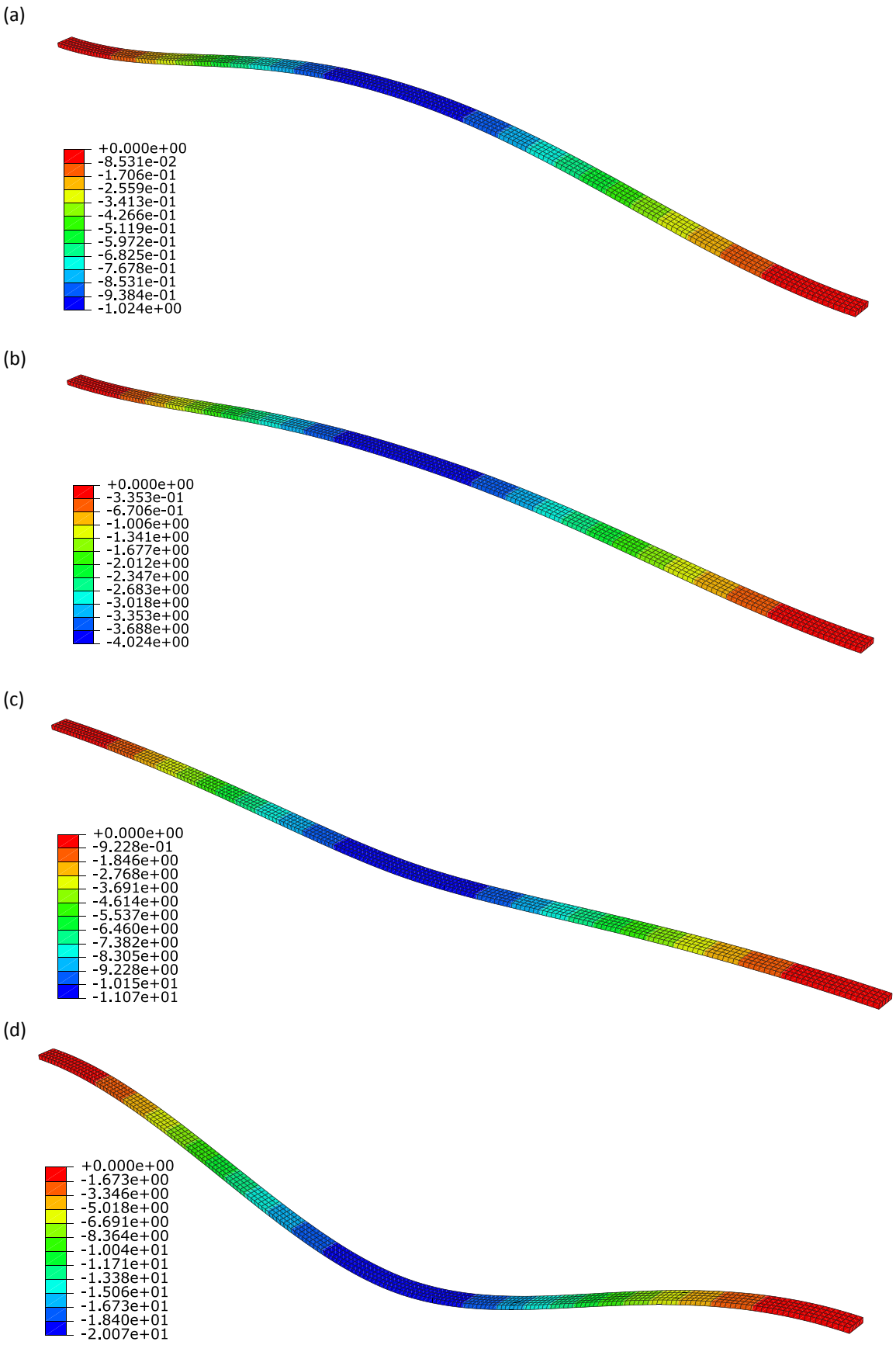

Fig.4. Contour plots of the deformed configuration of the initially curved beam with increasing midpoint force obtained using finite element analysis. A_0=0.05. The legends show the transverse displacement in mm.

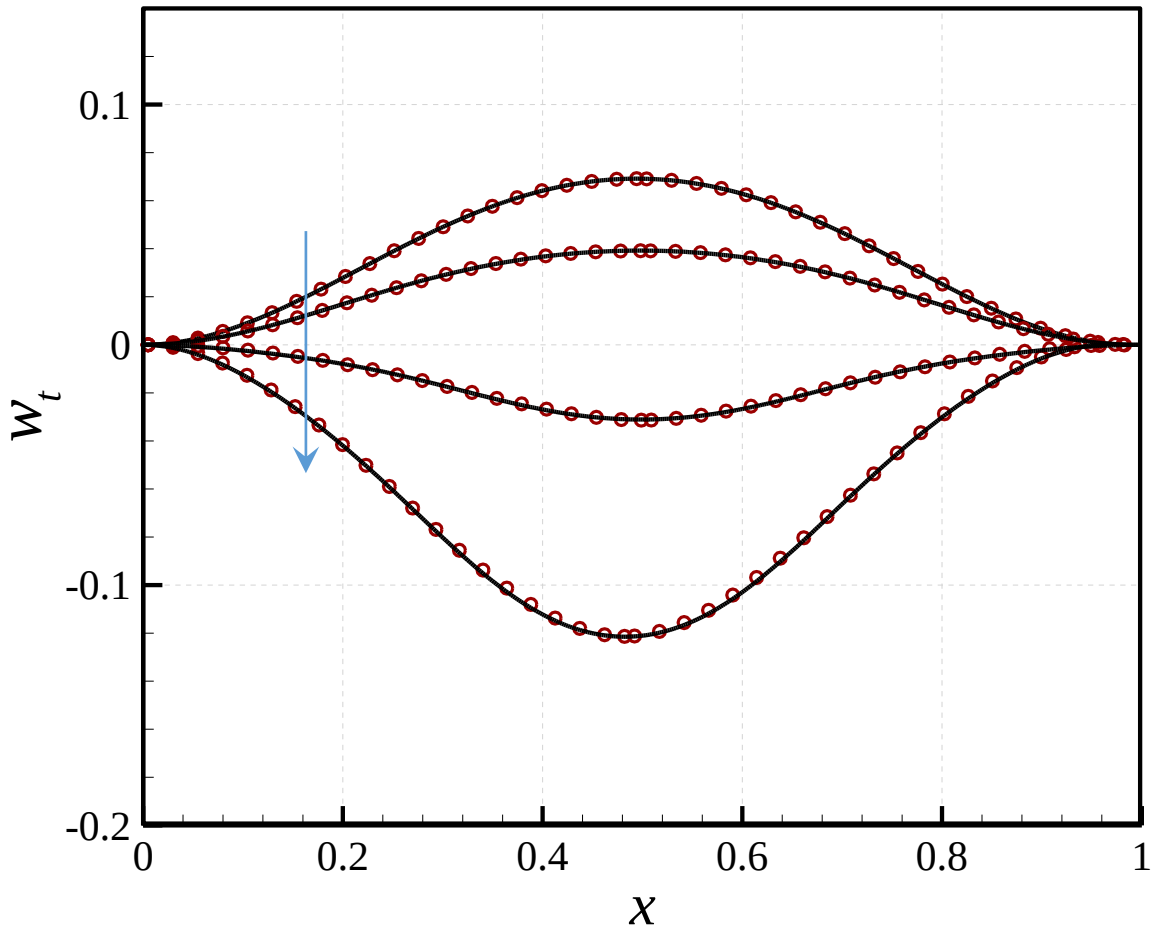

Fig.5. Deformed configuration of the initially curved beam obtained using the proposed model (solid line) and finite element analysis (symbols); A_0=0.05. The initially curved beam deform in the direction shown; deformed configurations are plotted for F=2.04, 7.87, 21.47, and 40.96.

(a)

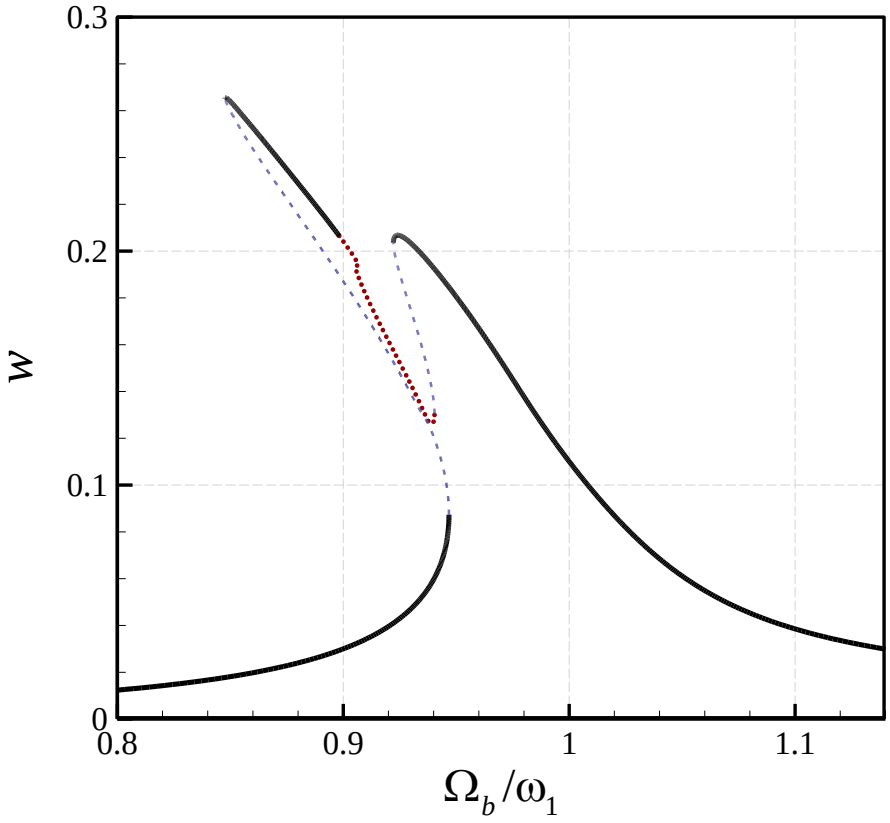
0.3
0.2
0.1
0
w
0.8
0.9
1
1.1
Ω_b/ω_1

(b)

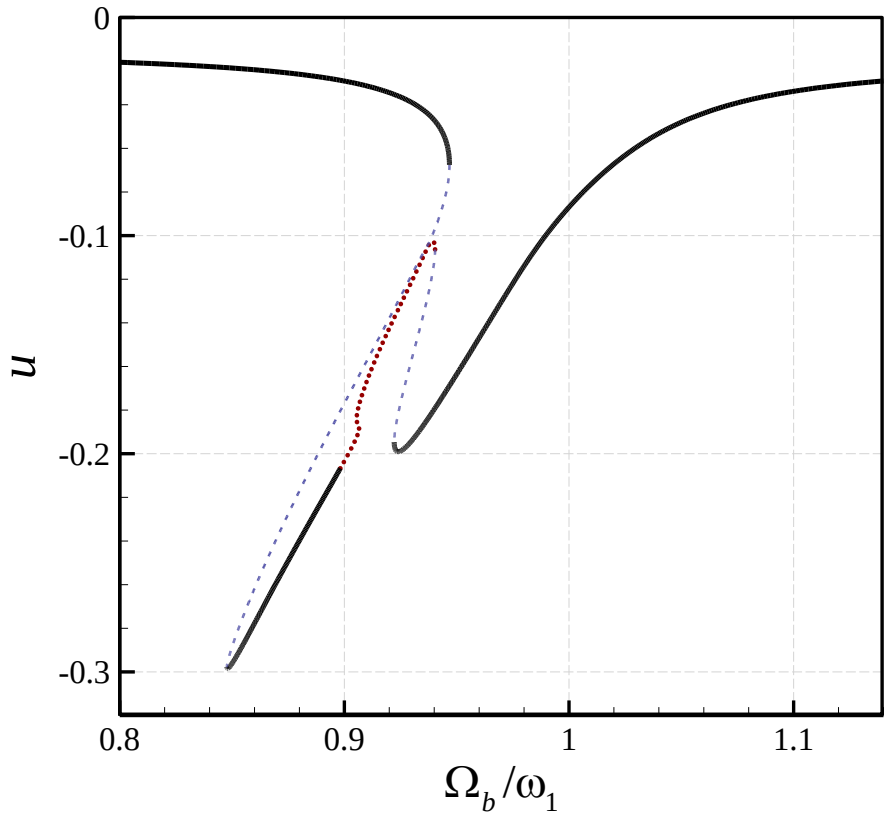
0
-0.1
-0.2
-0.3
u
0.8
0.9
1
1.1
Ω_b/ω_1

(c)

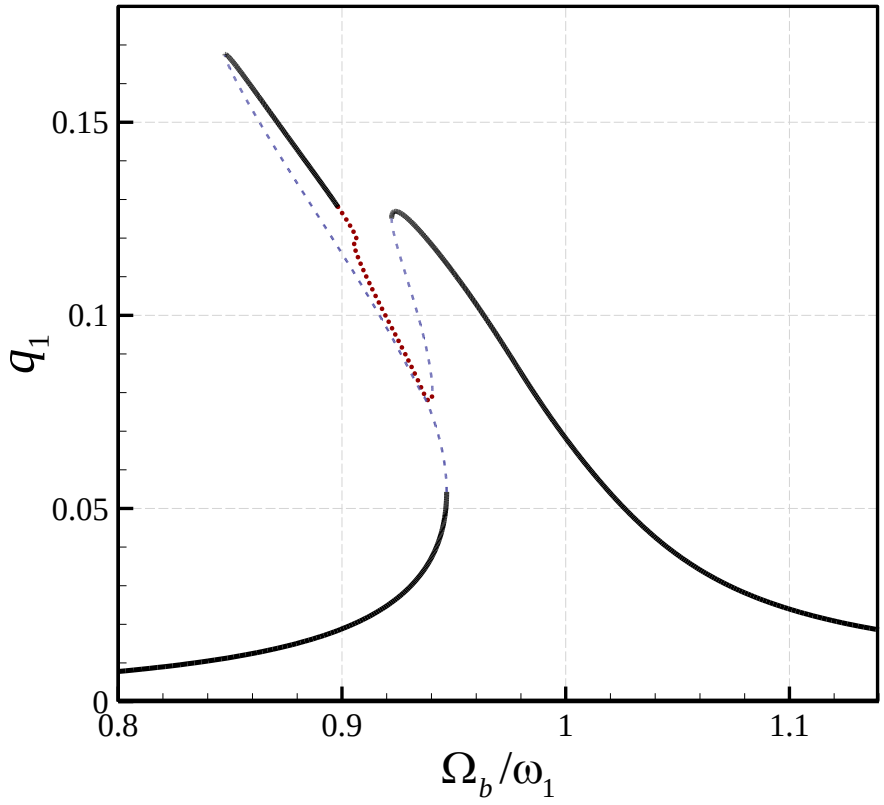

(d)

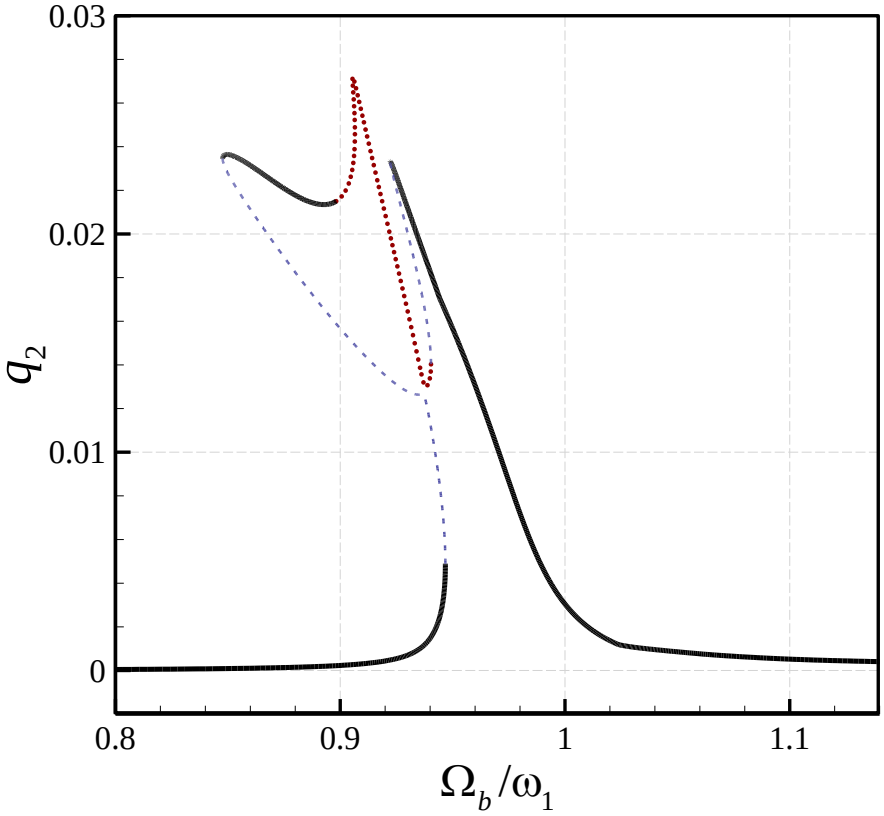

Fig.6. Amplitude-frequency plots of the unconstrained system; (a) w at x=0.5; (b) u at x=1.0; (c) q_1; (d) q_2; z_0=0.006 and A_0=0.05. Solid, dashed, and dotted lines: stable periodic, unstable periodic, and stable quasiperiodic responses, respectively.

(a)

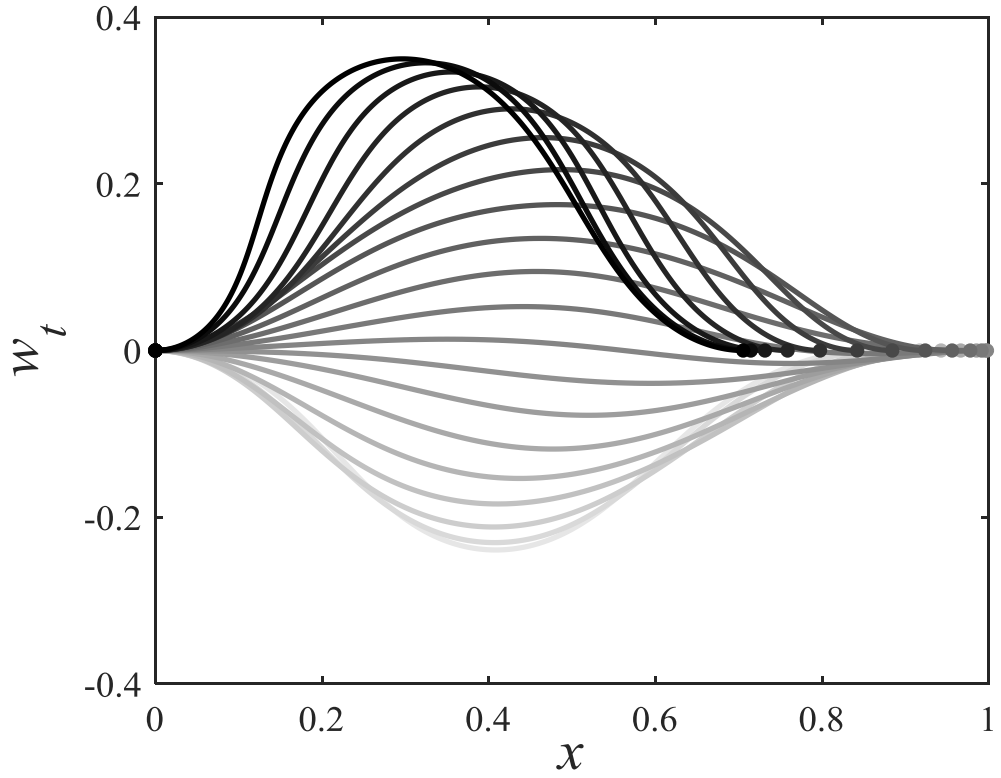

(b)

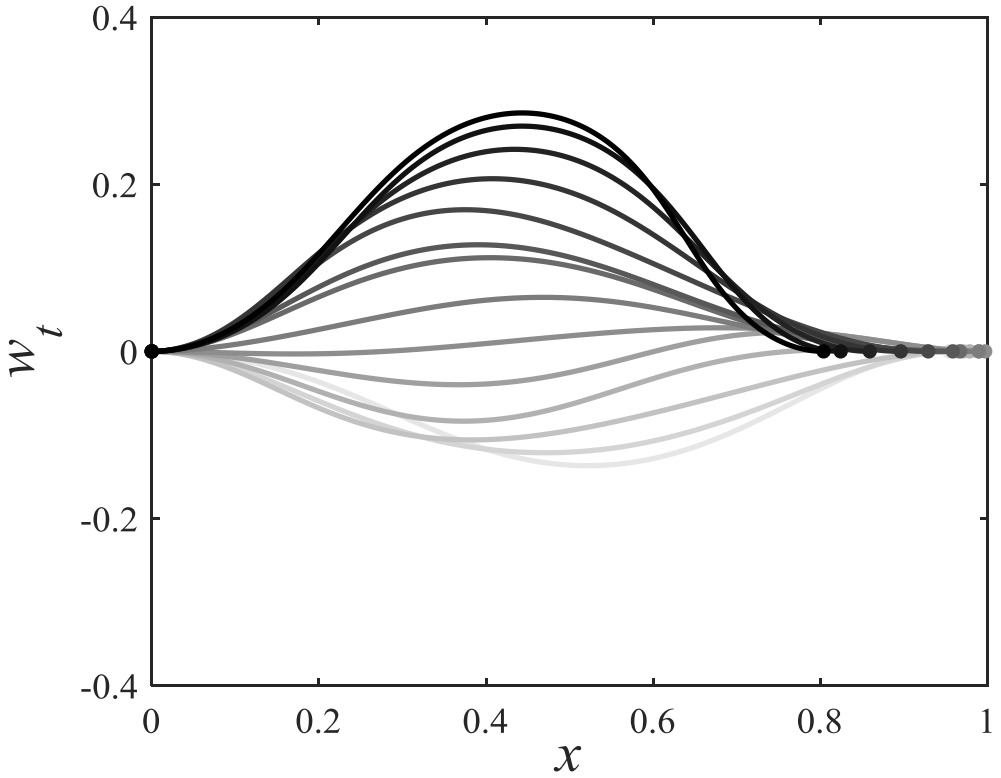

Fig.7. Oscillation of the unconstrained beam of Fig. 4 in one period at (a) Ω_b/ω_1 = 0.8477 (peak amplitude) and (b) Ω_b/ω_1 = 0.9225 (secondary peak); $w_t = w + w_0$.

(a)

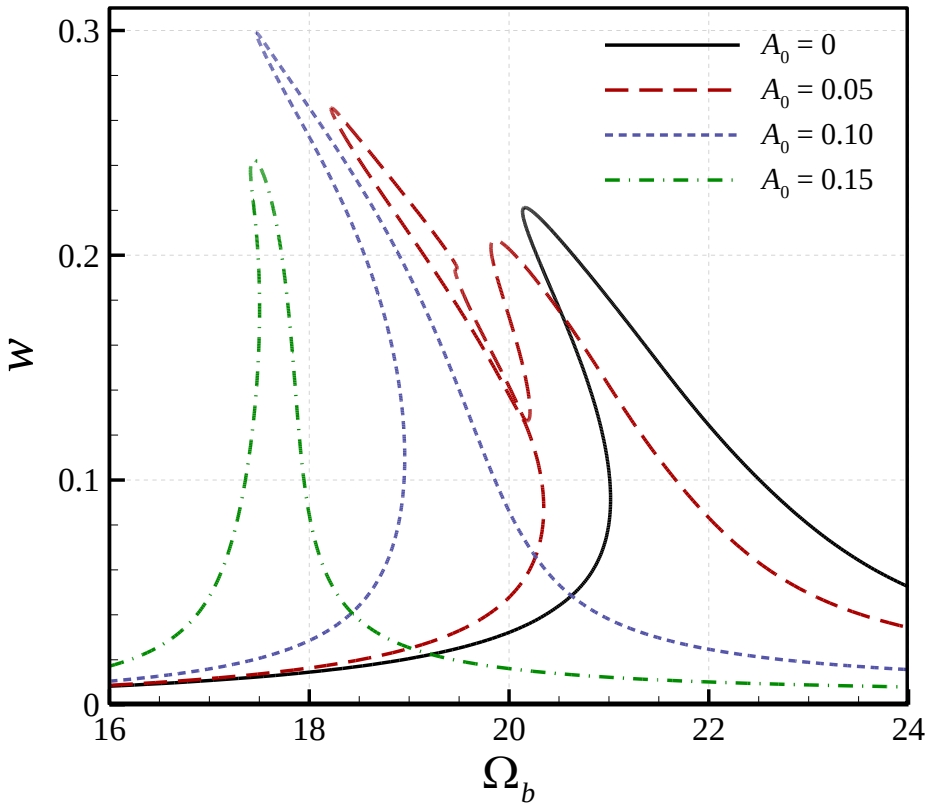

(b)

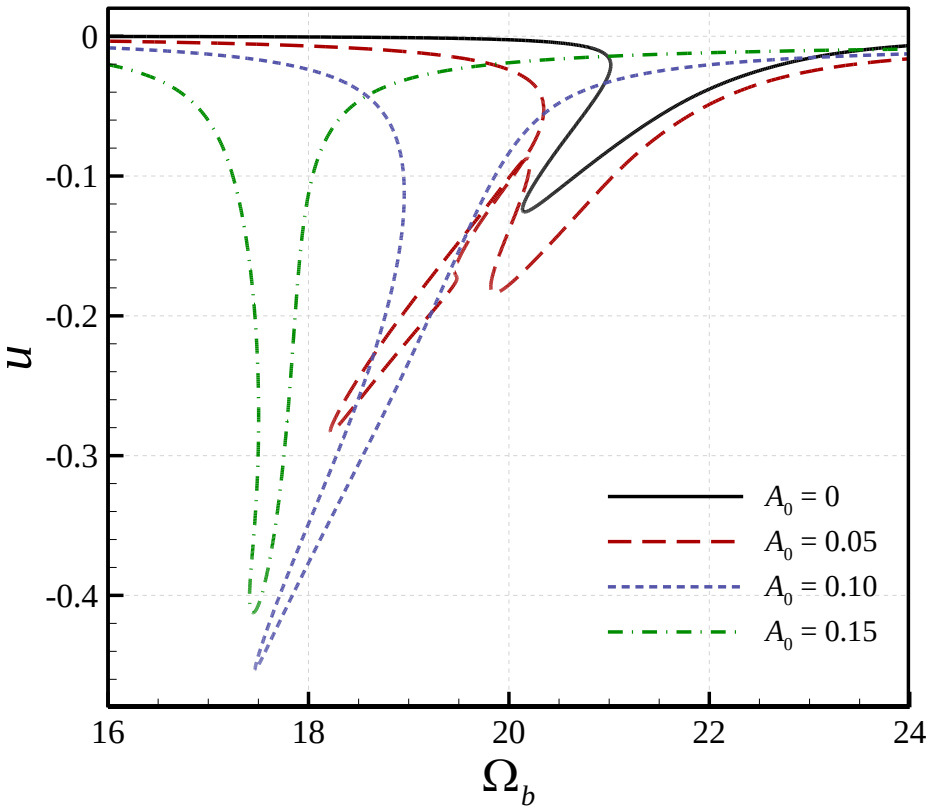

Fig.8. Amplitude-frequency plots of the unconstrained system for various initial curvature amplitudes; (a) *w* at *x*=0.5; (b) *u* at *x*=1.0; z_0=0.006.

(a)

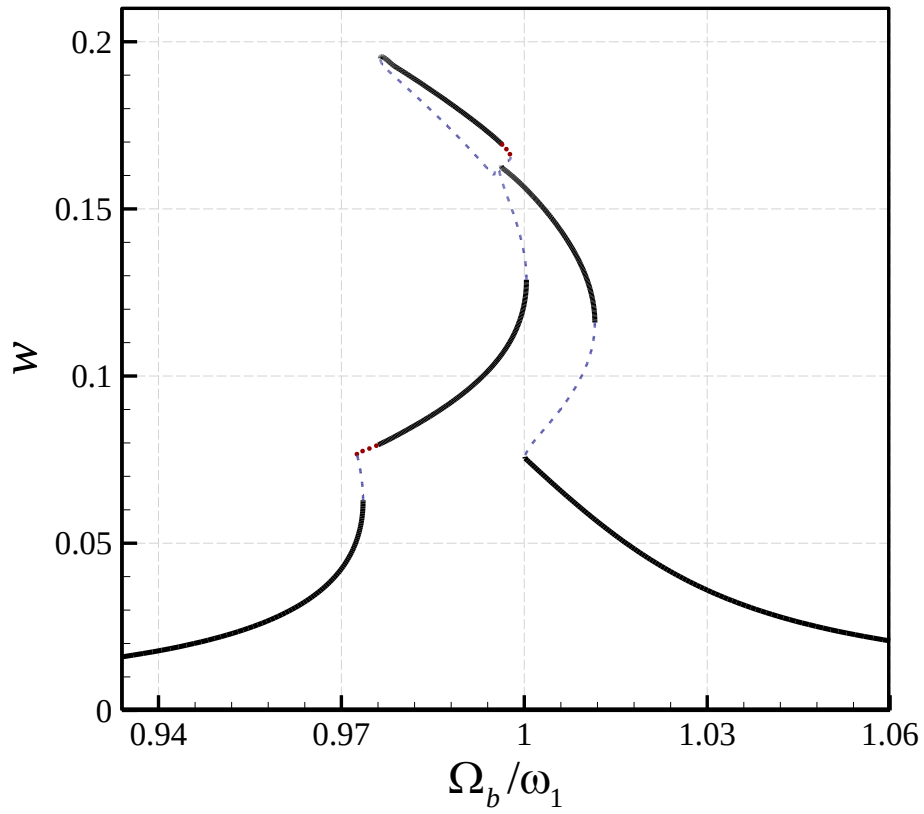

(b)

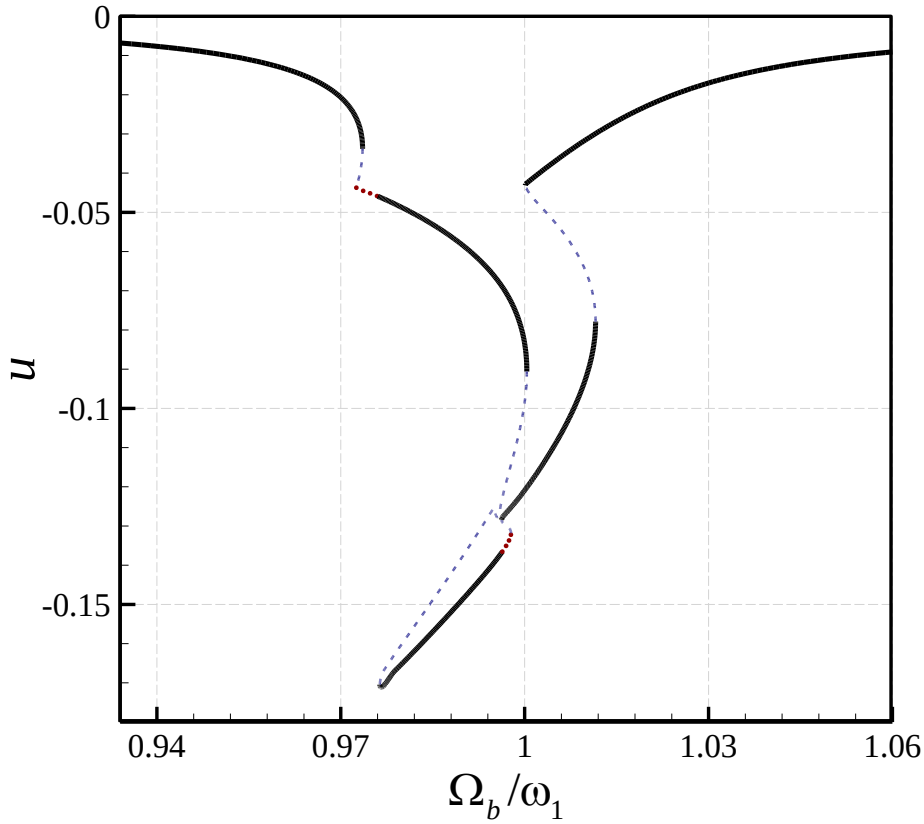

Fig.9. Amplitude-frequency plots of the constrained system; (a) w at x=0.5; (b) u at x=1.0; z_0=0.002, A_0=0.05, x_s=0.2, g_0=0.06, K_1=2.0×10^3, and K_3=2.0×10^6. Solid, dashed, and dotted lines: stable periodic, unstable periodic, and stable quasiperiodic responses, respectively.

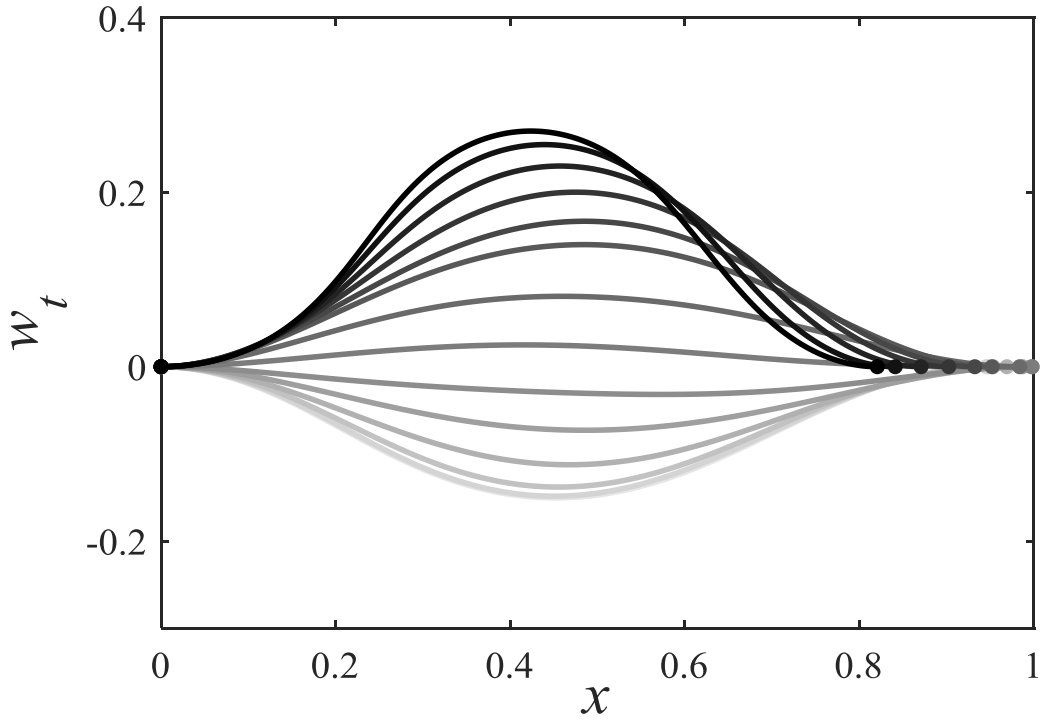

Fig.10. Oscillation of the constrained beam of Fig. 7 in one period at Ω_b/ω_1 = 0.9764 (peak amplitude); $w_t = w + w_0$.

(a)

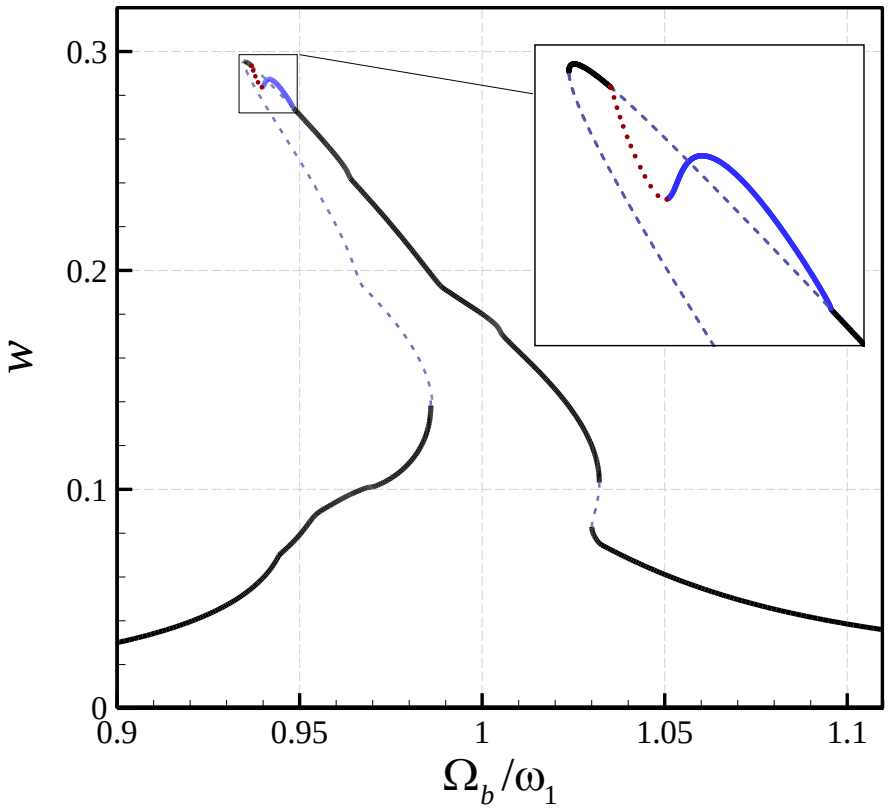

(b)

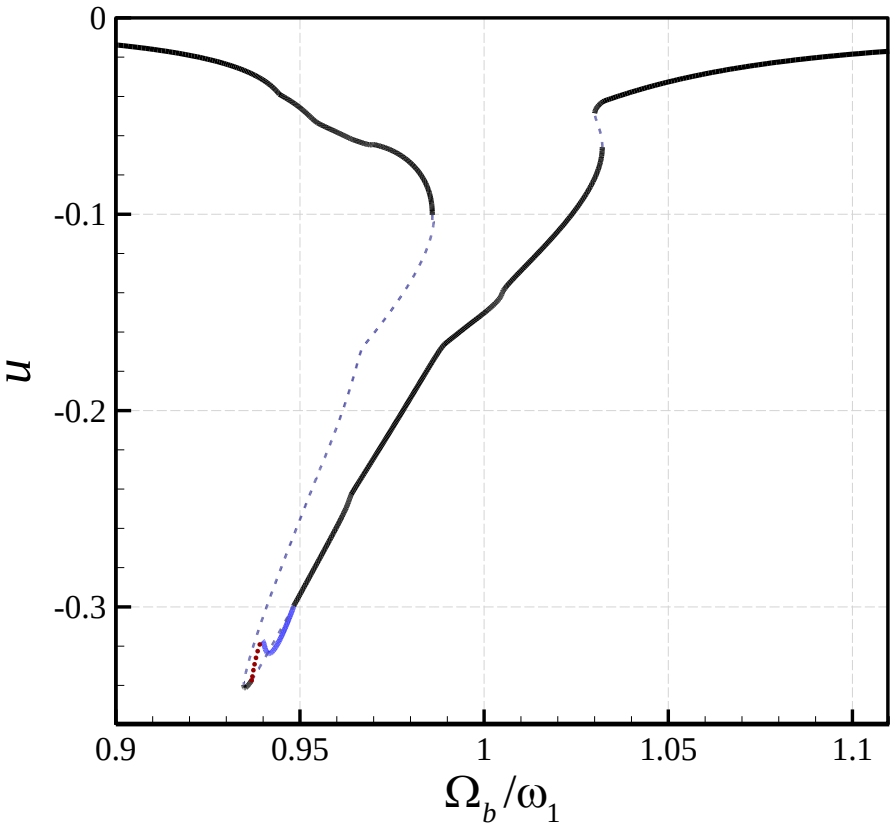

Fig.11. Amplitude-frequency plots of the constrained system; (a) w at x=0.5; (b) u at x=1.0; z_0=0.006, A_0=0.05, x_s=0.2, g_0=0.06, K_1=2.0×10^3, and K_3=2.0×10^6. Solid, dashed, and dotted lines: stable periodic, unstable periodic, and stable quasiperiodic responses, respectively.

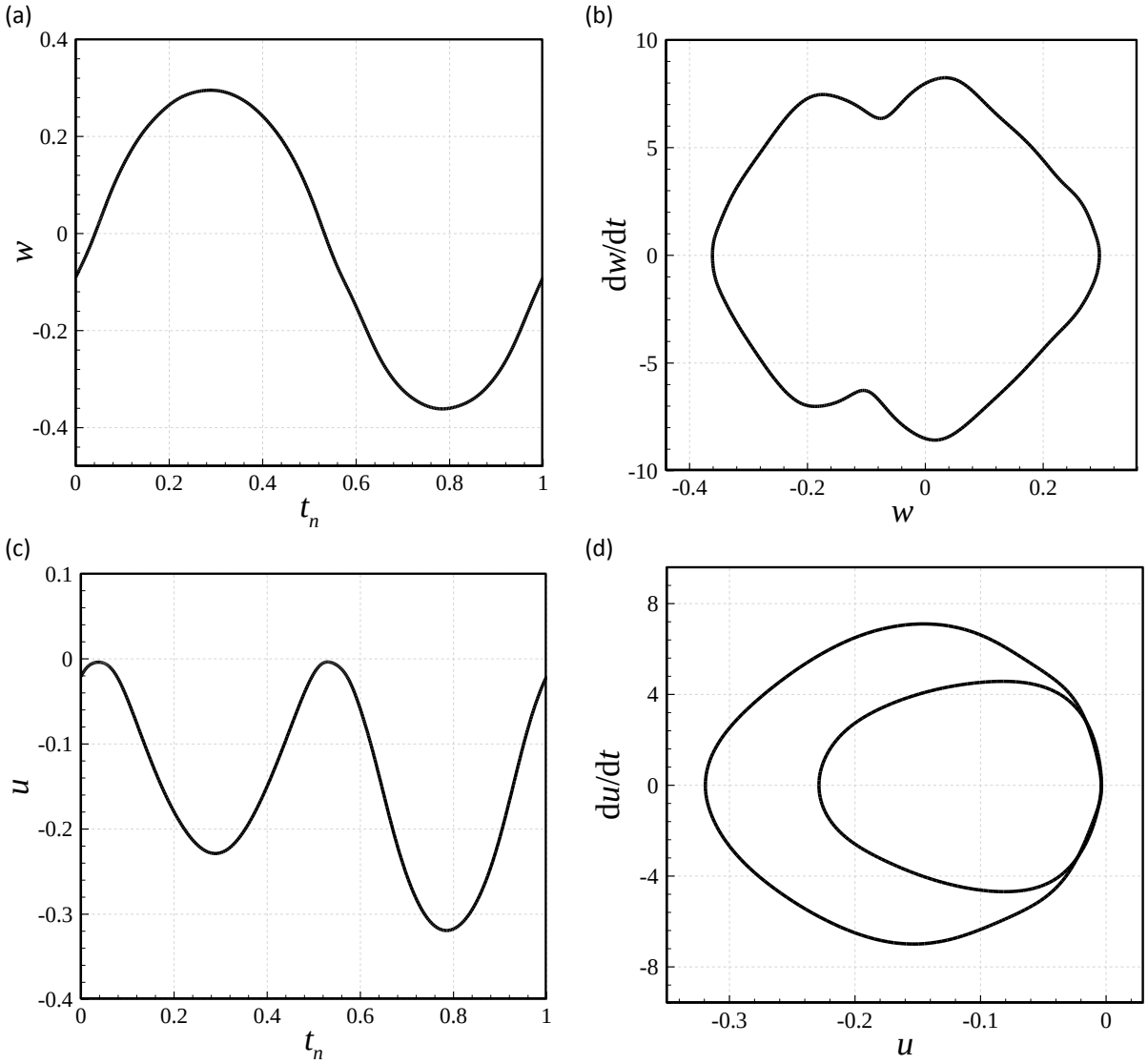

Fig.12. Vibration characteristics of the case of Fig. 9 at Ω_b/ω_1=0.9351 (peak amplitude), illustrating the time response and phase-plane plot of *w* at *x*=0.5 and those of *u* at *x*=1.0. t_n is the time normalised relative to oscillation period.

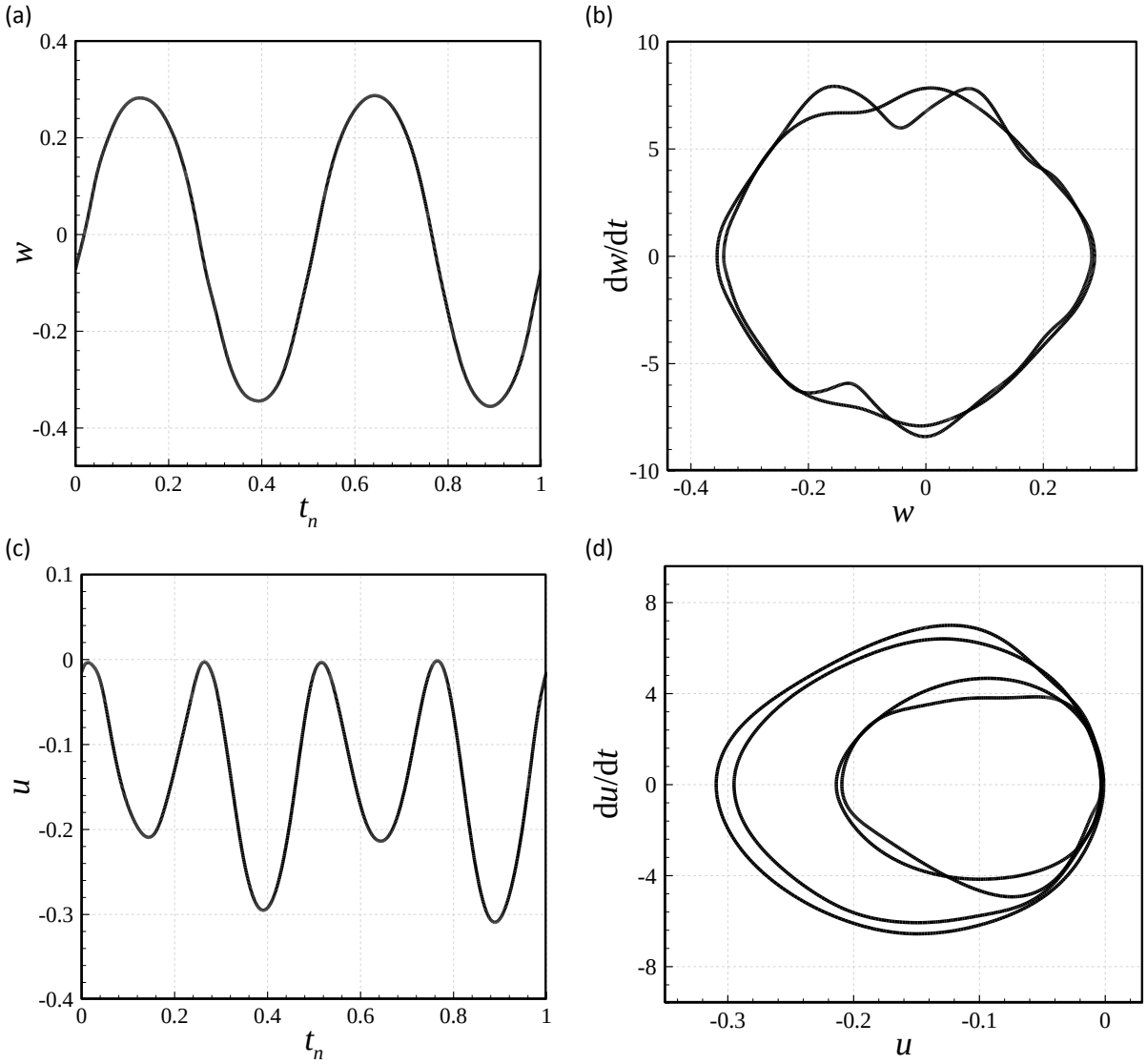

Fig.13. Vibration characteristics of the case of Fig. 9 at Ω_b/ω_1=0.9420 (bifurcated branch), illustrating the time response and phase-plane plot of *w* at *x*=0.5 and those of *u* at *x*=1.0. t_n is the time normalised relative to oscillation period.

(a)

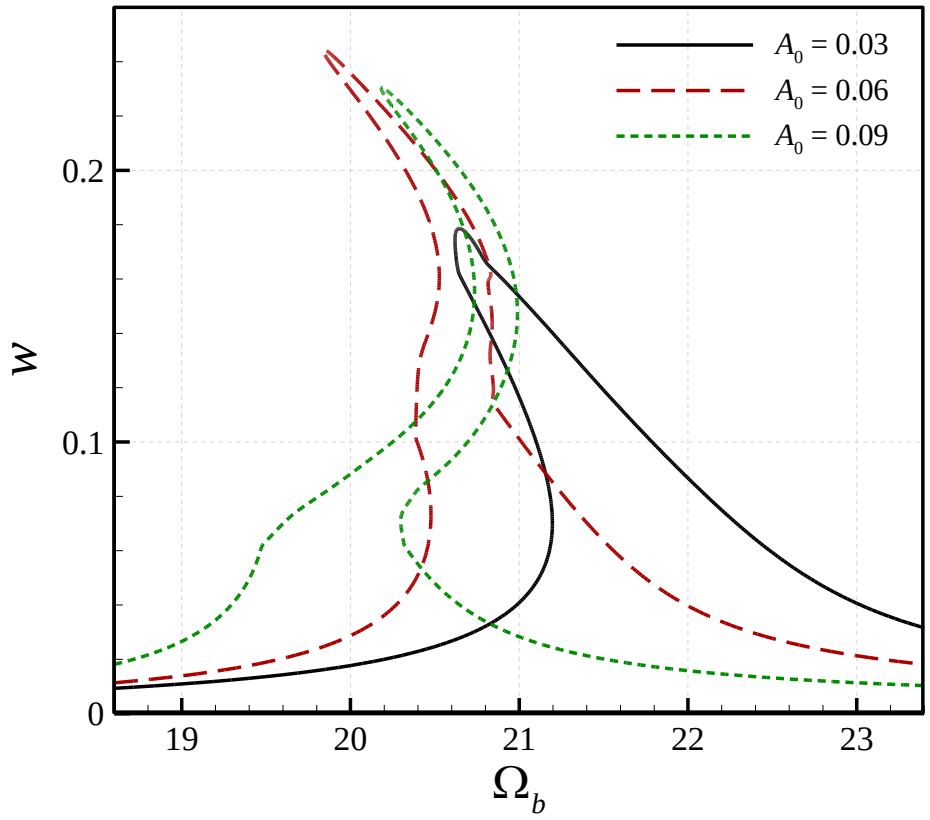

(b)

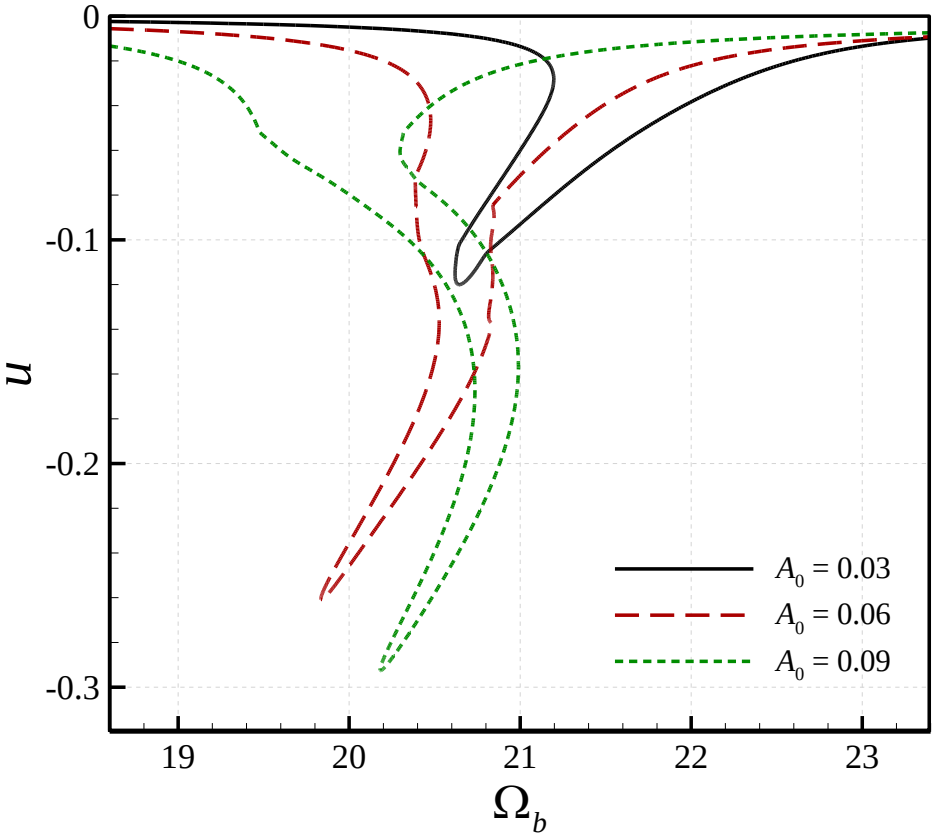

Fig.14. Amplitude-frequency plots of the constrained system for different initial curvature amplitudes; (a) w at x=0.5; (b) u at x=1.0; z_0=0.003, x_s=0.2, g_0=0.08, K_1=2.0×10^3, and K_3=2.0×10^6.

(a)

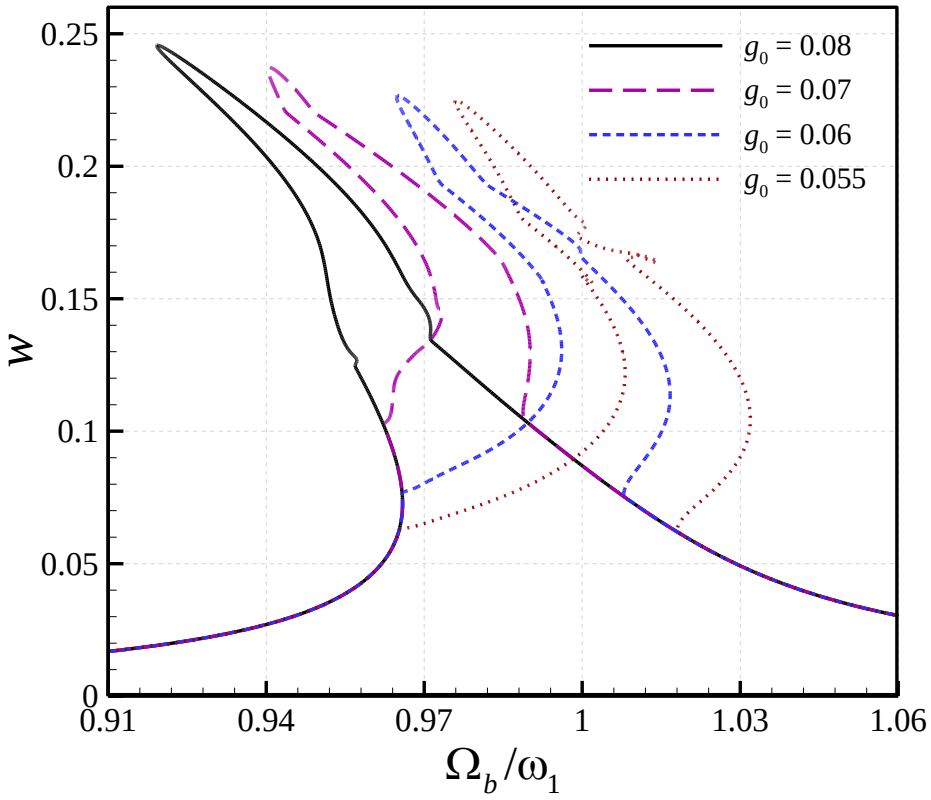

(b)

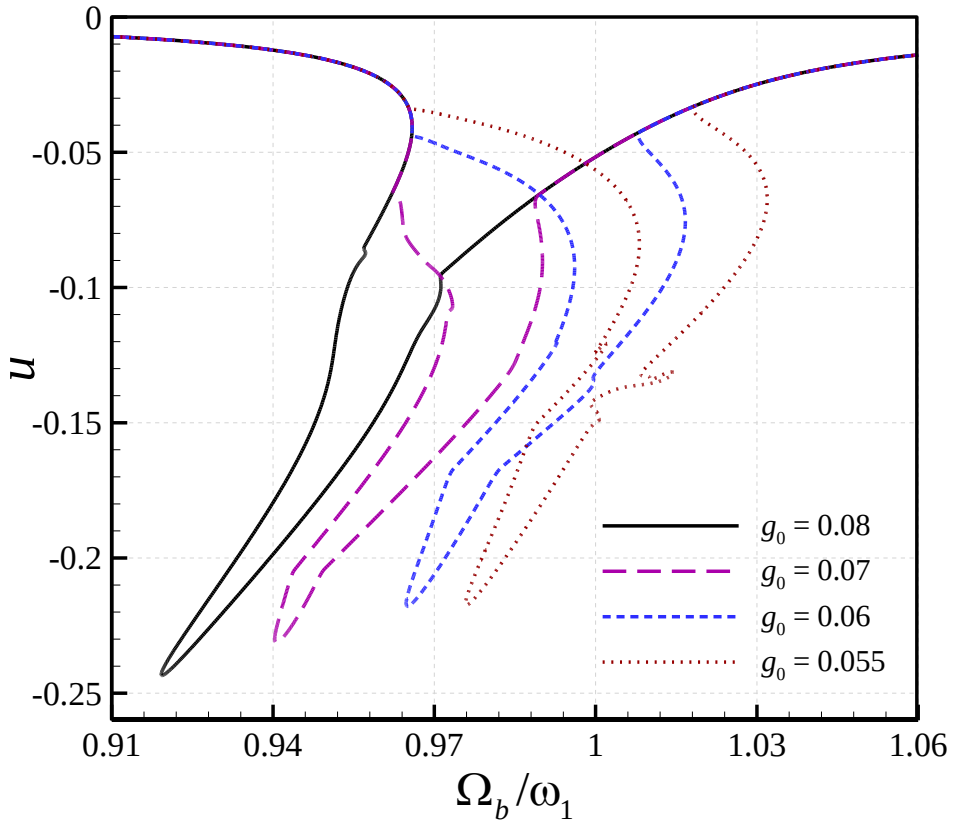

Fig.15. Amplitude-frequency plots of the constrained system for different values of the gap width; (a) w at x=0.5; (b) u at x=1.0; z_0=0.003, A_0=0.05, x_s=0.2, K_1=2.0×10^3, and K_3=2.0×10^6.

(a)

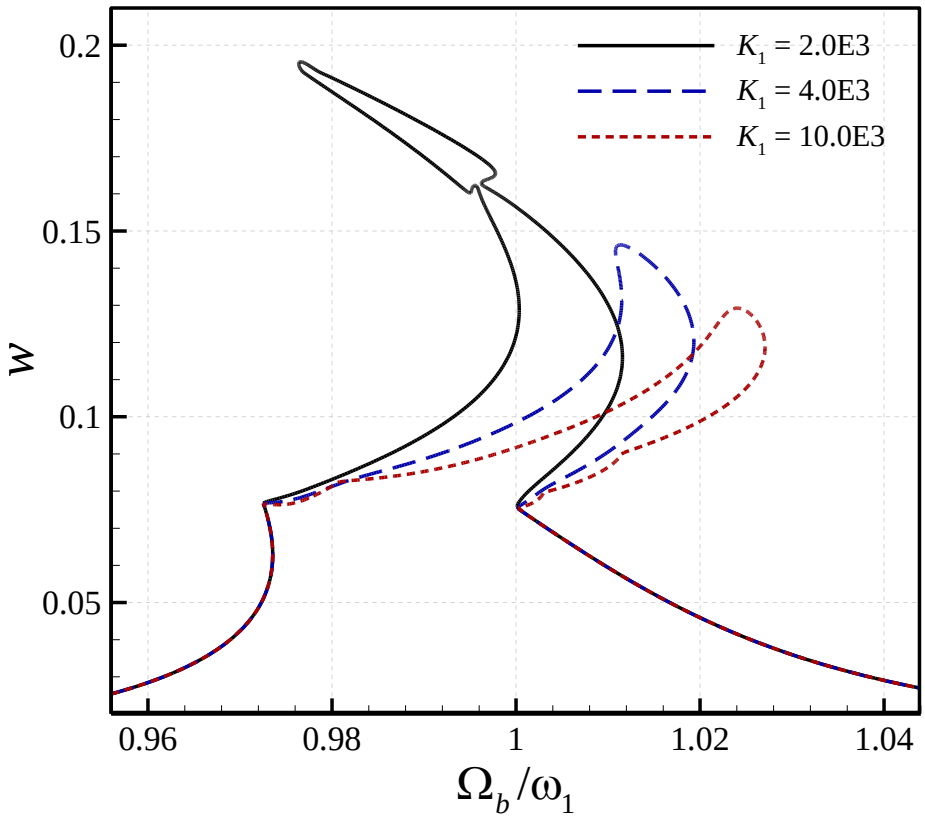

(b)

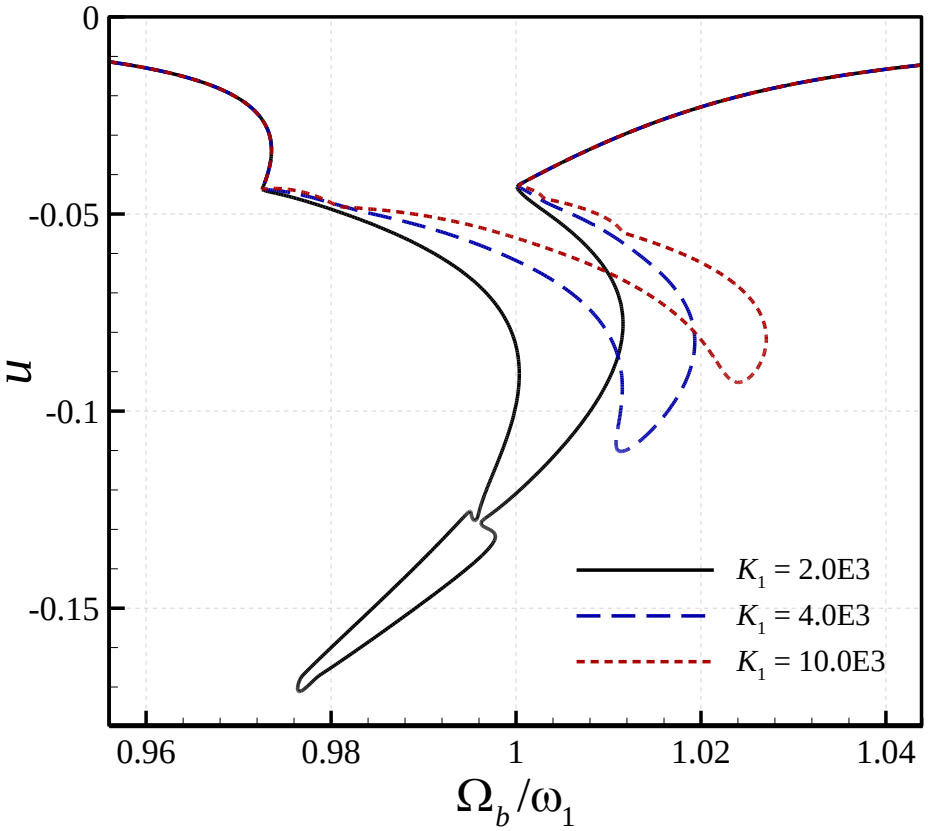

Fig.16. Amplitude-frequency plots of the constrained system for different coefficients of linear spring; (a) *w* at *x*=0.5; (b) *u* at *x*=1.0; z_0=0.002, A_0=0.05, x_s=0.2, g_0=0.06, and K_3=2.0×10^6.

(a)

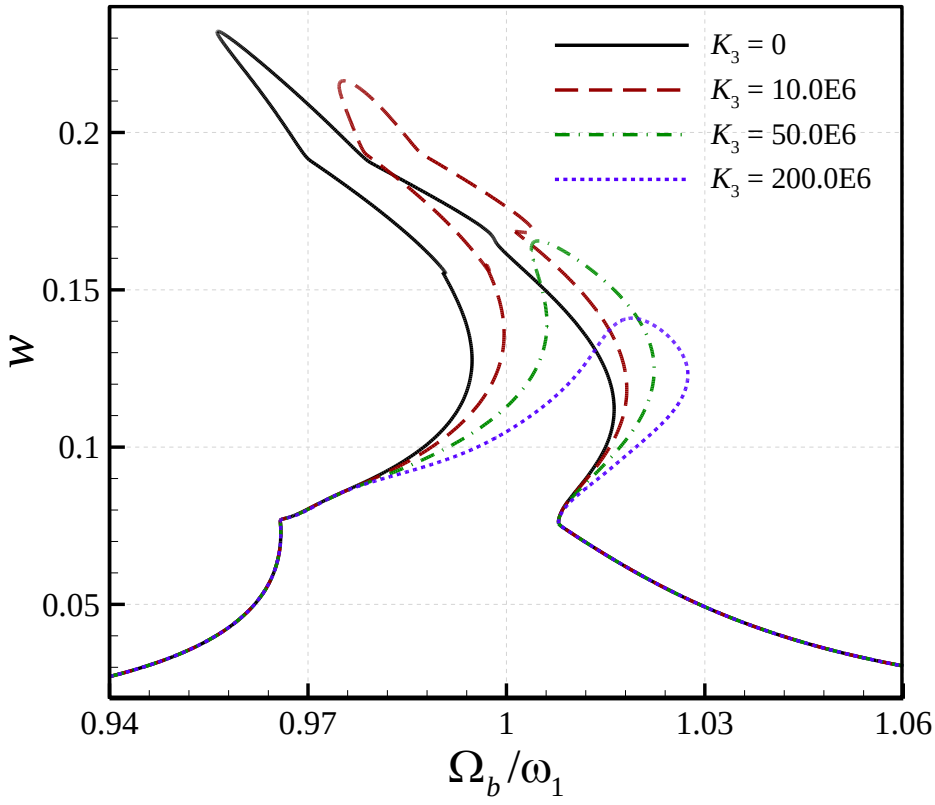

(b)

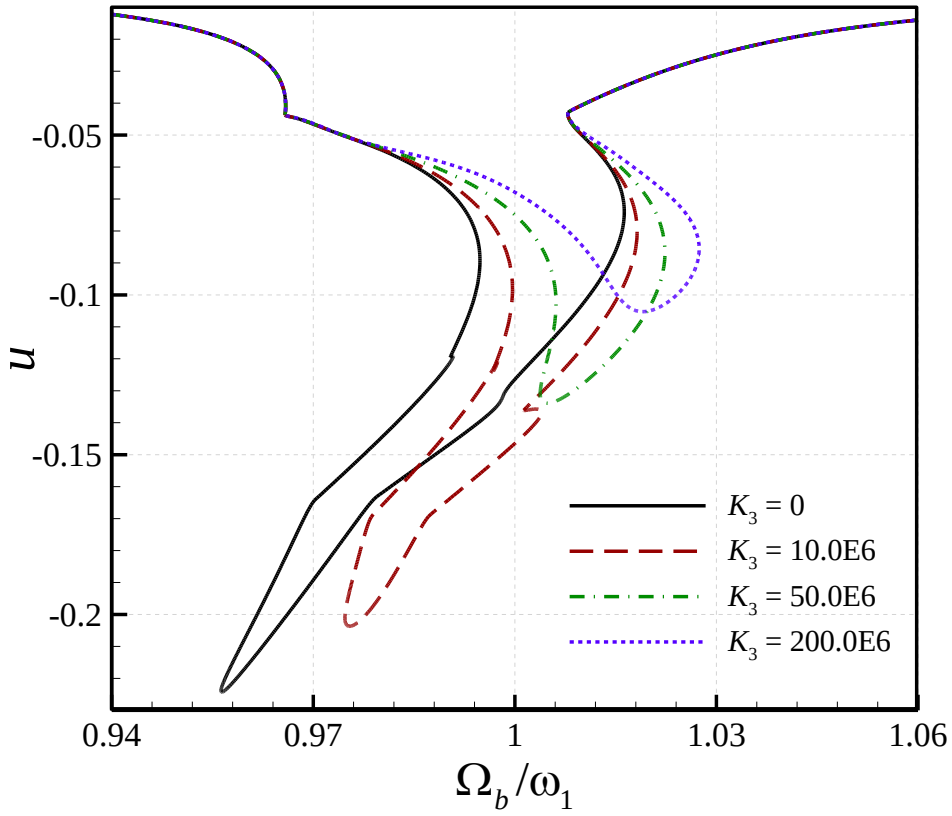

Fig.17. Amplitude-frequency plots of the constrained system for different coefficients of linear spring; (a) *w* at *x*=0.5; (b) *u* at *x*=1.0; z_0=0.003, A_0=0.05, x_s=0.2, g_0=0.06, and K_1=2.0×10^3.

(a)

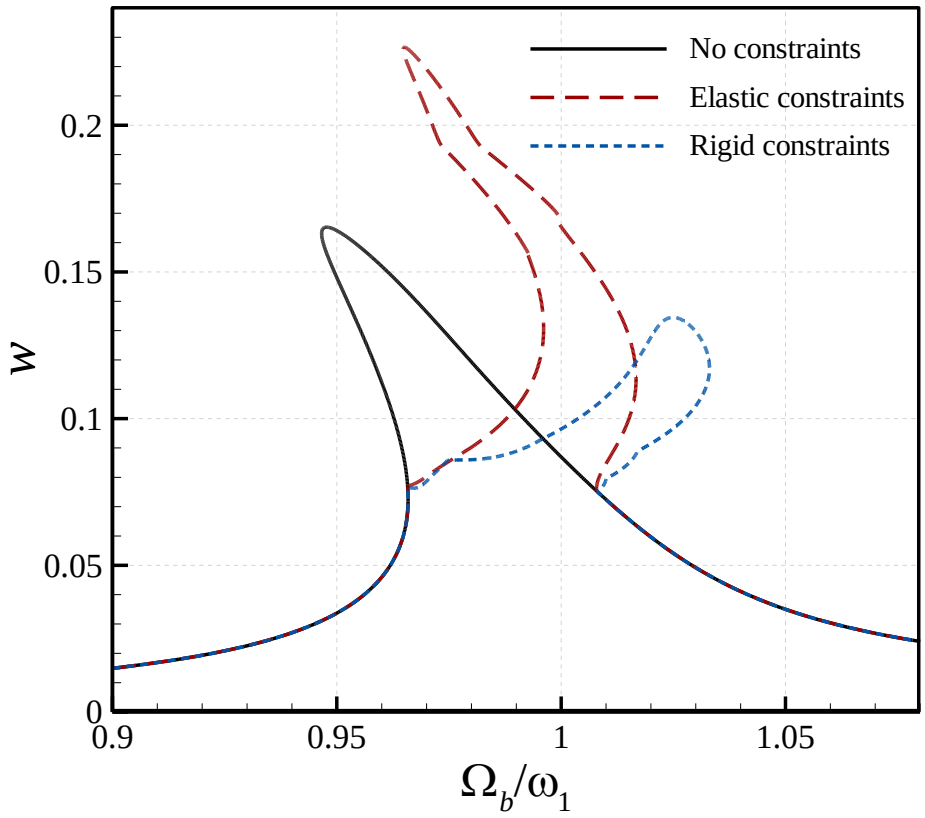

(b)

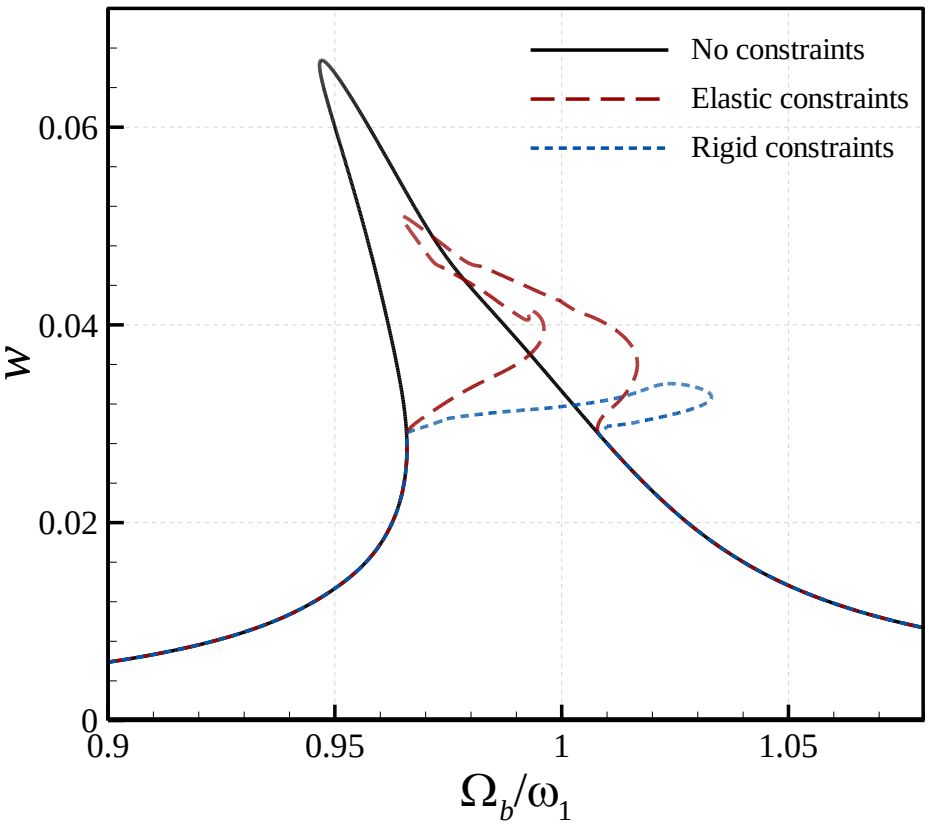

Fig.18. Comparison of amplitude-frequency curves of the unconstrained system to those of constrained systems; (a) w at x=0.5; (b) w at x=0.2; z_0=0.003, A_0=0.05, x_s=0.2, and g_0=0.06. K_1=2.0×10^3 and K_2=2.0×10^6 for the case "Elastic constraints"; K_1=10.0×10^3 and K_2=200.0×10^6 for the case "Rigid constraints".

(a)

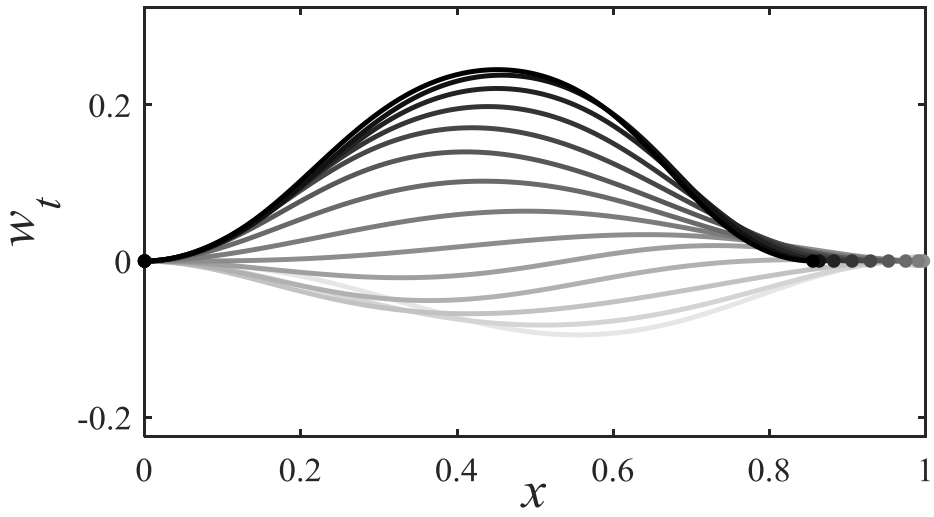

(b)

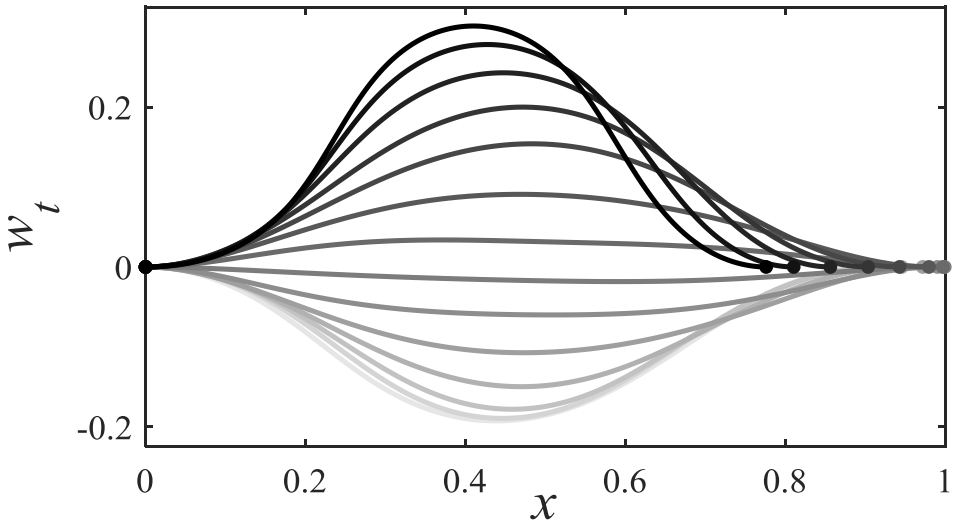

(c)

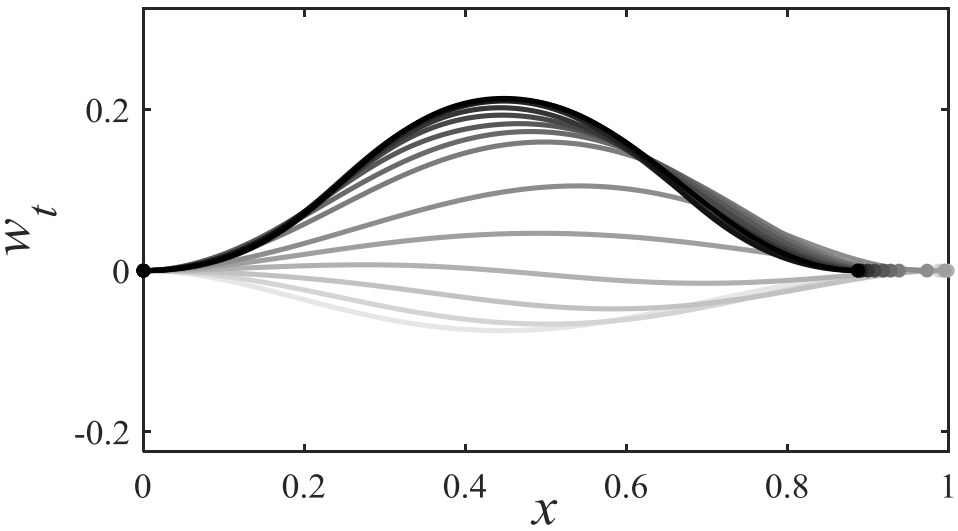

Fig.19. Vibration response of the three cases of Fig. 16, at points of peak amplitude; (a) No constraints; (b) Elastic constraints; (c) Rigid constraints.

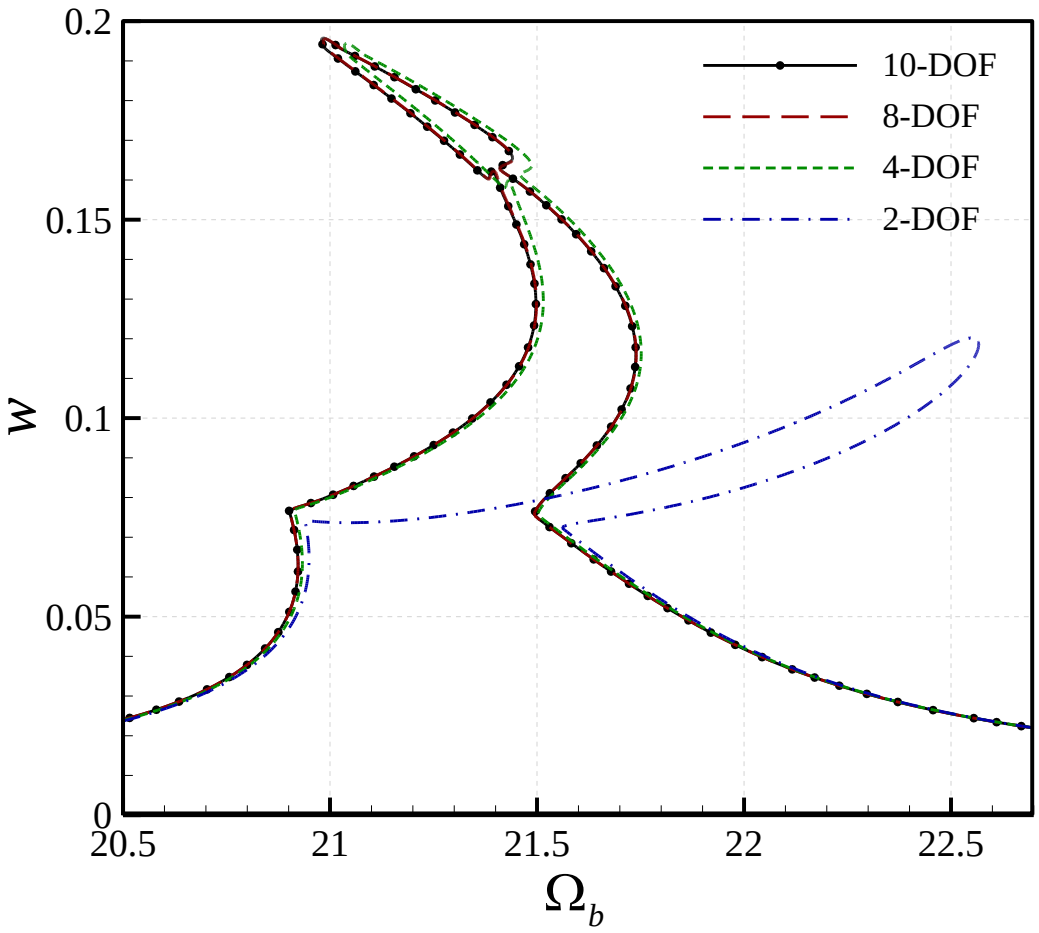

Fig.20. Amplitude-frequency plots of the constrained system for different discretised models showing w at x=0.5; z_0=0.002, A_0=0.05, x_s=0.2, g_0=0.06, K_1=2.0×10^3, and K_3=2.0×10^6.